

Thermoelectric performance of a minimally nonlinear voltage probe and voltage-temperature probe heat engine with broken time-reversal symmetry

Jayasmita Behera,¹ Salil Bedkihal,² Bijay Kumar Agarwalla,³ Malay Bandyopadhyay¹

¹*School of Basic Sciences, Indian Institute of Technology Bhubaneswar, Odisha, India 752050,*

²*Dartmouth Engineering Thayer School, 15 Thayer Drive, Hanover, NH 03755, USA,*

³*Department of Physics, Indian Institute of Science Education and Research, Pune 411008, India.*

(Dated: October 24, 2024)

We investigate the thermoelectric performance of a voltage probe and voltage-temperature probe minimally nonlinear irreversible heat engine with broken time-reversal symmetry by considering extended Onsager relations, where a nonlinear power dissipation term ($-\gamma_h J_L^{N^2}$) is added to the heat current. The analytical expressions for efficiency at a given power and efficiency at maximum power, in terms of asymmetry parameters and generalized figures of merit, are derived and analyzed. Our analysis with broken time-reversal symmetry and nonlinear effect reveals two universal bounds on the efficiency at maximum power (EMP) that overshoot the Curzon-Ahlborn (CA) limit. Although the analytical expressions of the bounds on EMP look similar, their respective Carnot efficiency and the asymmetry parameter set the difference between these heat engines which can be proved numerically. We consider a triple-dot Aharonov-Bohm heat engine with a voltage probe and voltage-temperature probe for our numerical simulation experiment. Unlike the voltage probe, the voltage-temperature probe heat engine requires an anisotropy in the system in addition to the magnetic field to break the time-reversal symmetry. In both probe cases, we observe high efficiency with low output power when the tunneling strength t is less than the coupling strength γ and vice-versa for $t > \gamma$. Our numerical experiment demonstrates that the efficiency at maximum output power and efficiency at a given power can be enhanced by increasing the power dissipation strength (γ_h) although the output power remains unaffected. The added nonlinear term helps us to surpass the CA limit of the upper bound on efficiency at maximum power for both cases with and without time-reversal symmetry.

PACS numbers: 85.25.Cp, 42.50.Dv

I. INTRODUCTION

The increasing demand to enhance energy conversion efficiency has driven interest in optimizing thermoelectric devices, with quantum coherence and broken time-reversal symmetry potentially offering new possibilities for improving their performance. Hence, there is a huge surge in the research on optimizing real-life thermodynamic cycles and designing efficient nanoscale thermoelectric heat engines for efficient energy harvesting [1–4]. Unlike bulk thermoelectrics, nanoscale heat engines perform heat-to-work conversion in steady-state without any macroscopic moving parts through steady-state flows of microscopic particles like electrons, photons, phonons, etc. Hence these thermal devices exhibit quantum interference effects which can induce and modify the thermoelectric response of a system [5–10]. The discrete energy levels of nanostructures based on a few quantum dots (QDs) or single molecular junctions provide energy filtering effects crucial for enhanced thermoelectric performance of quantum heat engines [8, 9, 11–23].

Improvement in the performance of a nanoscale heat engine demands a proper understanding of the fundamental thermodynamic constraints on the efficiency [24–29]. The efficiency of a thermoelectric reversible heat engine is bounded from above by the Carnot efficiency, $\eta_C = 1 - \frac{T_c}{T_h}$ [30], working between two heat reservoirs at temperatures T_h and T_c ($T_h > T_c$). However, an ideal reversible heat engine operates infinitely slowly to sat-

isfy reversibility resulting in zero output power. With the development of finite-time thermodynamics [31–36], Curzon and Ahlborn [31] proposed the efficiency at maximum power of a finite-time Carnot model widely known as Curzon-Ahlborn (CA) efficiency: $\eta_{CA} = 1 - \sqrt{T_c/T_h}$. Another important quantity to quantify the performance of a heat engine is the efficiency at maximum power and it has been extensively used in literature to study quantum heat engines and stochastic engines [7, 8, 37–39].

Usually, the presence of a magnetic field breaks the time-reversal symmetry of a system [40], however, this is not the case for noninteracting and purely metallic two-terminal systems, where the thermopower is an even function of the magnetic field due to the symmetry properties of the scattering matrix. A third terminal, specifically a voltage probe or a voltage-temperature probe, can introduce inelastic scattering effects in the noninteracting system creating asymmetric thermopower with respect to the magnetic field [41–44]. Within the linear irreversible framework, Brandner *et al.* proposed a strong bound on Onsager coefficients as a consequence of unitarity of scattering matrix for multiterminal thermoelectric heat engine with broken time-reversal symmetry [45–47]. Within the context of broken time-reversal symmetry, the efficiency at maximum power exceeds the CA limit for three-terminal and multi-terminal systems in the linear-response regime [45–52]. The study of three-terminal QDs-based heat engines shows enhanced thermoelectric performance in the linear-response regime [53, 54]. Recently, Zahra *et al.* showed that the volt-

age probe heat engine performs better than the voltage-temperature probe heat engine [55] in the linear response regime with broken time-reversal symmetry.

In the present manuscript, we extended the study of Zahra *et al.* for the minimally nonlinear irreversible heat engine. Izumida *et al.* first proposed a minimally nonlinear irreversible heat engine model that incorporates Onsager relations with an additional nonlinear dissipation term and obtained a new upper bound on the efficiency at maximum power, $\eta_+ = \eta_C/(2 - \eta_C)$ which exceeds the CA limit [56, 57]. The generality of the extended Onsager relations is validated by comparing it with the low-dissipation Carnot engine [36]. Several studies on these heat engines have been performed and the effect of dissipation on the efficiency and its upper bound is derived [58–62]. Within broken time-reversal symmetry, the upper bound on the efficiency and the efficiency at maximum power which exceeds the CA limit is derived in Ref. [63, 64]. Despite the studies mentioned above, a three-terminal heat engine with broken time-reversal symmetry working in the minimally nonlinear regime has not been investigated yet. This paper aims to optimize the thermoelectric performance and find out the upper bound on the efficiency at maximum power for a minimally nonlinear three-terminal heat engine with broken time-reversal symmetry incorporating a Buttiker voltage probe or a voltage-temperature probe.

Initially, we consider a generalized three-terminal system subjected to an external magnetic field and connected to three fermionic reservoirs (L, P, R) maintained at different temperatures and chemical potentials as shown in Fig. 1. The third reservoir could be (i) a voltage probe that blocks the net particle current but allows the heat current to the probe [44, 55, 65–68] or (ii) a voltage-temperature probe that blocks both particle and heat currents to the probe to introduce inelastic scattering effects into the system [44, 46–48, 50, 52, 55]. A nonlinear term ($-\gamma_h J_L^N$) meaning the power dissipation is added to the linear Onsager relation for heat current with γ_h denoting the strength of dissipation to the hot reservoir and J_L^N is the particle current flowing from the left reservoir. The efficiency at a given power and efficiency at maximum power of the voltage probe and the voltage-temperature probe heat engine are characterized by the parameters x, x_m, y, y_m, d_m , and α where x and x_m are the asymmetry parameter and y and y_m are the generalized figure of merit for the voltage-temperature probe and the voltage probe heat engine, respectively. The parameter d_m is defined for the voltage probe heat engine denoting the thermal conductance and temperature bias ratio. Here $m = L$ and $m = LP$ correspond to the case where the heat current from reservoir L and both L and P are absorbed by the scattering region, respectively. The dimensionless parameter α denotes the dissipation strength ratio. Within the context of broken time-reversal symmetry, we obtain a universal upper bound on the efficiency at maximum power for a mini-

mally nonlinear voltage probe heat engine as follows:

$$\eta_m^*(P_{max}) = \frac{\eta_{C,m}(P_{max})x_m^2}{2(2x_m^2 - 3x_m + 2) - \alpha T X_L^T x_m^2}, \quad (1)$$

where $\eta_{C,m}(P_{max})$ is the Carnot efficiency derived at the point of maximum power for the voltage probe heat engine. Note that the Carnot efficiency for a voltage probe heat engine depends on the heat currents detailed in appendix C. The upper bound for the minimally nonlinear voltage-temperature probe heat engine is obtained as

$$\eta^*(P_{max}) = \frac{\eta_C x^2}{2(2x^2 - 3x + 2) - \alpha T X_L^T x^2}. \quad (2)$$

The difference between the bounds obtained for the above two heat engines is characterized by their respective Carnot efficiency and asymmetry parameters which can be analyzed numerically. By setting $\alpha = 0$, the linear-response results are recovered [52, 55]. Note that we consider two types of nonlinearities: (a) the nonlinear response of the conductor due to many-body interactions, modeled through probes at the mean-field level, and (b) the inclusion of the nonlinear (Joule heating) term. As a result, our analysis extends beyond the non-interacting regime.

To explicitly demonstrate our derived results for a generalized three-terminal system, we perform a numerical simulation for a triple-dot Aharonov-Bohm (AB) heat engine comprised of three quantum dots arranged in a triangular geometry with dot 2 either connected to a voltage probe or voltage-temperature probe (see Fig. 2). The AB interferometer is widely investigated as a phase tunable quantum device and a broken time-reversal symmetric system [44, 65, 69–76]. The triangular geometry of triple-dot AB interferometer can exhibit higher-order quantum interference effects [77]. In our recent paper [76], we have investigated the thermoelectric performance of a two-terminal triple-dot AB heat engine and obtained a significantly high value of $0.8\eta_C$ for efficiency at maximum power in the nonlinear regime which motivates us to investigate the system for the three-terminal setup in the minimally nonlinear regime. We demonstrate the tunability of the device by controlling the t/γ ratio in three regimes i.e., (a) $t/\gamma < 1$, (b) $t/\gamma = 1$, and (c) $t/\gamma > 1$ with t and γ denoting the inter-dot tunneling strength and dot-reservoir coupling strength, respectively. Note that the coupling strength γ differs from the dissipation strength γ_h .

The numerical results of our paper can be summarized as follows: (i) In the presence of a nonvanishing magnetic field, unlike the voltage probe heat engine, the voltage-temperature heat engine requires an anisotropy in the system, e.g., nondegenerate QDs ($\epsilon_1 \neq \epsilon_3$) to break the time-reversal symmetry of the system (see Ref. [48, 50]). (ii) We obtain higher efficiency with lower power output when $t/\gamma < 1$. The opposite trend is observed when $t/\gamma > 1$. (iii) The output power and efficiency are higher at zero magnetic flux i.e., for the time-reversal symmetric case. (iv) The efficiency at a given power and the

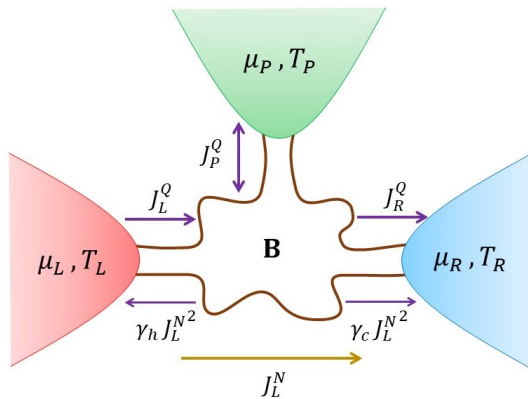


FIG. 1. Schematic illustration of a minimally nonlinear three-terminal heat engine with broken time-reversal symmetry. The arrows show the direction of the particle current (J_L^N), heat currents (J_L^Q , J_P^Q , and J_R^Q), and the dissipation terms $\gamma_h J_L^N^2$ and $\gamma_c J_L^N^2$ included in the heat fluxes J_L^Q and J_R^Q , respectively.

efficiency at maximum power increase with increasing the power dissipation strength ratio α although the output power remains unaffected. (v) The power-efficiency trade-off for the voltage probe and voltage-temperature probe heat engines are very similar since $y_m/d_m \sim y$. (vi) The normalized efficiency is higher and attains maximum value at a power relatively smaller than the maximum power in the favorable branch. (vii) The CA limit on the efficiency at maximum power is exceeded with broken time-reversal symmetry and the introduction of nonlinearity makes it faster to overcome the CA limit even in the time-reversal symmetry case.

The rest of the paper is organized as follows: We introduce a general three-terminal model and develop linear Onsager relations between the currents and the thermodynamic biases in Sec. II. Section III elaborates on the minimally nonlinear voltage probe and voltage-temperature probe heat engines utilizing extended Onsager relations. A triple-dot AB heat engine is investigated in Sec. IV and the numerical results are discussed in Sec. V. We conclude in Sec. VI. Additional detailed calculations are presented in Appendix A, B, and C.

II. MODEL AND FORMULATION

This section is dedicated to a brief theoretical background on linear irreversible thermodynamics and the phenomenological equation connecting the fluxes with the thermodynamic forces described as $\mathbf{J} = \mathcal{L}\mathbf{X}$. We use the Büttiker probe technique i.e., (i) voltage probe and (ii) voltage-temperature probe, to simulate inelastic scattering effects into the system [41–44, 65–68]. Further, strong bounds on the Onsager coefficients are obtained

in the subsequent section.

A. Linear irreversible three-terminal heat engine

A three-terminal thermoelectric heat engine with broken time-reversal symmetry is depicted in Fig. 1. A scattering region subjected to an external magnetic field \mathbf{B} is connected to three different fermionic reservoirs termed as left (L), right (R), and probe (P) that can exchange both heat and particles with the system. The temperature and chemical potential of the left and right reservoirs are set as $T_L > T_R$ and $\mu_L < \mu_R$ to ensure our system works as a thermoelectric heat engine. The probe parameters (T_P , μ_P) are adjusted to block particle flow or both particle and heat flow. We assume the right reservoir as a reference by setting $(\mu_R, T_R) = (\mu, T)$ and write $\mu_\nu = \mu + \Delta\mu_\nu$, $T_\nu = T + \Delta T_\nu$ for $\nu = L, P$. Our system operates in the linear response regime if $|\Delta\mu_\nu/T| \ll 1$ and $|\Delta T_\nu/T| \ll 1$. The particle currents (J_ν^N) and the energy currents (J_ν^U) flowing from the reservoir ν satisfy the current conservation laws i.e., $\sum_\nu J_\nu^{N(U)} = 0$. The heat current (J_ν^Q) flowing from the reservoir ν can be expressed in terms of J_ν^N and J_ν^U as $J_\nu^Q = J_\nu^U - \mu_\nu J_\nu^N$. Considering the above conditions, one can linearly expand the particle and heat currents defined in Eqs. (A1) and (A2) and obtain the linear Onsager relation between the thermodynamic fluxes (particle and heat currents) and forces (chemical potential and temperature biases) as $\mathbf{J} = \mathcal{L}\mathbf{X}$ [46, 48, 50, 52, 53, 55]:

$$\begin{pmatrix} J_L^N \\ J_L^Q \\ J_P^N \\ J_P^Q \end{pmatrix} = \begin{pmatrix} \mathcal{L}_{11} & \mathcal{L}_{12} & \mathcal{L}_{13} & \mathcal{L}_{14} \\ \mathcal{L}_{21} & \mathcal{L}_{22} & \mathcal{L}_{23} & \mathcal{L}_{24} \\ \mathcal{L}_{31} & \mathcal{L}_{32} & \mathcal{L}_{33} & \mathcal{L}_{34} \\ \mathcal{L}_{41} & \mathcal{L}_{42} & \mathcal{L}_{43} & \mathcal{L}_{44} \end{pmatrix} \begin{pmatrix} X_L^\mu \\ X_L^T \\ X_P^\mu \\ X_P^T \end{pmatrix}, \quad (3)$$

where $X_\nu^\mu = (\mu_\nu - \mu_R)/T_R$ and $X_\nu^T = 1/T_R - 1/T_\nu$ ($X_\nu^T \approx \Delta T_\nu/T^2$) for $\nu = L, P$ are the generalized forces. Here \mathcal{L} is 4×4 Onsager matrix and its elements \mathcal{L}_{ij} are called the Onsager coefficients and we will suppress \mathbf{B} in the Onsager coefficients to keep the notation simple, unless necessary. The explicit expressions of the Onsager coefficients are given in Appendix A.

B. Voltage probe and voltage-temperature probe heat engine

The voltage probe introduces dissipative inelastic scattering processes into the system by demanding that the net particle current flowing to the probe vanishes (i.e., $J_P^N = 0$) but allowing a nonzero heat current ($J_P^Q \neq 0$) from the probe [44, 55, 65–68]. Thus, from Eq. (3), we can be derived X_P^μ as follows:

$$X_P^\mu = -\frac{(\mathcal{L}_{31}X_L^\mu + \mathcal{L}_{32}X_L^T + \mathcal{L}_{34}X_P^T)}{\mathcal{L}_{33}}. \quad (4)$$

Substituting Eq. (4) in Eq. (3) and after some algebra we can express the currents in terms of a (3×3) reduced Onsager matrix \mathcal{L}' as follows [55]:

$$\begin{pmatrix} J_L^N \\ J_L^Q \\ J_P^Q \end{pmatrix} = \begin{pmatrix} \mathcal{L}'_{11} & \mathcal{L}'_{12} & \mathcal{L}'_{13} \\ \mathcal{L}'_{21} & \mathcal{L}'_{22} & \mathcal{L}'_{23} \\ \mathcal{L}'_{31} & \mathcal{L}'_{32} & \mathcal{L}'_{33} \end{pmatrix} \begin{pmatrix} X_L^\mu \\ X_L^T \\ X_P^T \end{pmatrix}, \quad (5)$$

where the reduced Onsager coefficients \mathcal{L}'_{ij} are expressed as follows [55]:

$$\begin{aligned} \mathcal{L}'_{11} &= \frac{\mathcal{L}_{33}\mathcal{L}_{11} - \mathcal{L}_{13}\mathcal{L}_{31}}{\mathcal{L}_{33}}, & \mathcal{L}'_{12} &= \frac{\mathcal{L}_{33}\mathcal{L}_{12} - \mathcal{L}_{13}\mathcal{L}_{32}}{\mathcal{L}_{33}}, \\ \mathcal{L}'_{13} &= \frac{\mathcal{L}_{33}\mathcal{L}_{14} - \mathcal{L}_{13}\mathcal{L}_{34}}{\mathcal{L}_{33}}, & \mathcal{L}'_{21} &= \frac{\mathcal{L}_{33}\mathcal{L}_{21} - \mathcal{L}_{23}\mathcal{L}_{31}}{\mathcal{L}_{33}}, \\ \mathcal{L}'_{22} &= \frac{\mathcal{L}_{33}\mathcal{L}_{22} - \mathcal{L}_{23}\mathcal{L}_{32}}{\mathcal{L}_{33}}, & \mathcal{L}'_{23} &= \frac{\mathcal{L}_{33}\mathcal{L}_{24} - \mathcal{L}_{23}\mathcal{L}_{34}}{\mathcal{L}_{33}}, & (6) \\ \mathcal{L}'_{31} &= \frac{\mathcal{L}_{33}\mathcal{L}_{41} - \mathcal{L}_{43}\mathcal{L}_{31}}{\mathcal{L}_{33}}, & \mathcal{L}'_{32} &= \frac{\mathcal{L}_{33}\mathcal{L}_{42} - \mathcal{L}_{43}\mathcal{L}_{32}}{\mathcal{L}_{33}}, \\ & & \mathcal{L}'_{33} &= \frac{\mathcal{L}_{33}\mathcal{L}_{44} - \mathcal{L}_{43}\mathcal{L}_{34}}{\mathcal{L}_{33}}. \end{aligned}$$

Likewise, for a voltage-temperature probe, the chemical potential and the probe's temperature are adjusted so that both the net particle current and heat current from the probe vanishes i.e., $J_P^N = 0$ and $J_P^Q = 0$ [44, 46, 48, 50, 52, 55]. We can obtain a (2×2) reduced Onsager matrix \mathcal{L}'' for the voltage-temperature probe by setting $J_P^Q = 0$ in Eq. (5) and it is expressed as follows [55]:

$$\begin{pmatrix} J_L^N \\ J_L^Q \end{pmatrix} = \begin{pmatrix} \mathcal{L}''_{11} & \mathcal{L}''_{12} \\ \mathcal{L}''_{21} & \mathcal{L}''_{11} \end{pmatrix} \begin{pmatrix} X_L^\mu \\ X_L^T \end{pmatrix}, \quad (7)$$

where the reduced Onsager coefficients for the voltage-temperature probe are

$$\begin{aligned} \mathcal{L}''_{11} &= \frac{\mathcal{L}'_{33}\mathcal{L}'_{11} - \mathcal{L}'_{13}\mathcal{L}'_{31}}{\mathcal{L}'_{33}}, & \mathcal{L}''_{12} &= \frac{\mathcal{L}'_{33}\mathcal{L}'_{12} - \mathcal{L}'_{13}\mathcal{L}'_{32}}{\mathcal{L}'_{33}}, \\ \mathcal{L}''_{21} &= \frac{\mathcal{L}'_{33}\mathcal{L}'_{21} - \mathcal{L}'_{23}\mathcal{L}'_{31}}{\mathcal{L}'_{33}}, & \mathcal{L}''_{22} &= \frac{\mathcal{L}'_{33}\mathcal{L}'_{22} - \mathcal{L}'_{23}\mathcal{L}'_{32}}{\mathcal{L}'_{33}}. \end{aligned} \quad (8)$$

The time-reversal symmetry is broken in the presence of a nonzero magnetic field and the Onsager coefficients follow the Onsager-Casimir relation [78]

$$\mathcal{L}'_{ij}(\mathbf{B}) = \mathcal{L}'_{ji}(-\mathbf{B}) \quad \text{and} \quad \mathcal{L}''_{ij}(\mathbf{B}) = \mathcal{L}''_{ji}(-\mathbf{B}). \quad (9)$$

C. Bounds on the Onsager coefficients

Onsager coefficients are subject to some constraints due to the second law of thermodynamics which can be derived from the positivity of the entropy production rate for a two-terminal heat engine [40]. However, for a multi-terminal system ($n \geq 3$) with broken time-reversal symmetry, the unitarity of the scattering matrix imposes

stronger bounds on Onsager coefficients than that of the positivity of entropy production rate [45, 46]. So, the reduced Onsager coefficients for the voltage probe heat engine satisfy the following inequalities [55]:

$$\begin{aligned} \mathfrak{L}_{11} &\geq 0, & \mathfrak{L}_{22} &\geq 0, \\ \mathfrak{L}_{11}\mathfrak{L}_{22} + \mathfrak{L}_{12}\mathfrak{L}_{21} - \mathfrak{L}_{12}^2 - \mathfrak{L}_{21}^2 &\geq 0, \end{aligned} \quad (10)$$

where

$$\begin{aligned} \mathfrak{L}_{11} &= \mathcal{L}'_{11}, \\ \mathfrak{L}_{12} &= \mathcal{L}'_{12} + \mathcal{L}'_{13}\xi, \\ \mathfrak{L}_{21} &= \mathcal{L}'_{21} + \mathcal{L}'_{31}\xi, \\ \mathfrak{L}_{22} &= \mathcal{L}'_{22} + \mathcal{L}'_{33}\xi^2 + (\mathcal{L}'_{23} + \mathcal{L}'_{32})\xi, \end{aligned} \quad (11)$$

with $\xi = X_P^T/X_L^T$. Similarly, the Onsager bounds for the voltage-temperature probe heat engine [45, 46, 55] are

$$\begin{aligned} \mathcal{L}''_{11} &\geq 0, & \mathcal{L}''_{22} &\geq 0, \\ \mathcal{L}''_{11}\mathcal{L}''_{22} + \mathcal{L}''_{12}\mathcal{L}''_{21} - \mathcal{L}''_{12}^2 - \mathcal{L}''_{21}^2 &\geq 0. \end{aligned} \quad (12)$$

III. MINIMALLY NONLINEAR THREE-TERMINAL HEAT ENGINE

We consider a minimally nonlinear irreversible heat engine model which accounts for possible thermal dissipation effects due to the interaction between the system and the reservoir [56–64]. A nonlinear term $-\gamma_h J_L^{N^2}$ meaning power dissipation is added to the linear Onsager relation for the heat current from the left reservoir (J_L^Q) described in Eqs. (5) and (7). Here $-\gamma_h J_L^{N^2}$ denotes the dissipation to the hot reservoir (left) and $\gamma_h (> 0)$ is the strength of dissipation [56, 57]. The addition of this nonlinear term can be treated as a natural extension of the linear irreversible heat engine. We assume that no other higher-order nonlinear terms contribute to the currents. The dissipation is assumed to be weak, so the bounds on the Onsager coefficients discussed in Eq. (10) and Eq. (12) still hold for the minimally nonlinear heat engine model. Unlike the linear response regime, the generalized forces are not restricted to small values for the minimally nonlinear heat engine. Considering the above assumptions we discuss the thermoelectric performance of the minimally nonlinear heat engine with voltage probe and voltage-temperature probe in the subsequent sections.

A. Voltage probe heat engine

The extended Onsager relations for the minimally nonlinear voltage probe heat engine are expressed as follows:

$$\begin{aligned} J_L^N &= \mathcal{L}'_{11}X_L^\mu + \mathcal{L}'_{12}X_L^T + \mathcal{L}'_{13}X_P^T, \\ J_L^Q &= \mathcal{L}'_{21}X_L^\mu + \mathcal{L}'_{22}X_L^T + \mathcal{L}'_{23}X_P^T - \gamma_h J_L^{N^2}, \\ J_P^Q &= \mathcal{L}'_{31}X_L^\mu + \mathcal{L}'_{32}X_L^T + \mathcal{L}'_{33}X_P^T. \end{aligned} \quad (13)$$

The linear Onsager relations are recovered by putting $\gamma_h = 0$. The nonlinear term ($-\gamma_h J_L^{N^2}$) represents the inevitable power loss due to the finite time operation of the heat engine [79, 80]. Since J_L^N and X_L^μ are uniquely related at a fixed values of X_L^T and X_P^T , we can choose J_L^N as our control parameter instead of X_L^μ by the relation

$$X_L^\mu = \frac{J_L^N - (\mathcal{L}'_{12} + \mathcal{L}'_{13}\xi)X_L^T}{\mathcal{L}'_{11}}, \quad (14)$$

where $\xi = X_P^T/X_L^T$. The output power, $P = -T_R X_L^\mu J_L^N > 0$ can be expressed by using J_L^N as

$$P = \frac{T_R}{\mathcal{L}'_{11}} (\mathcal{L}'_{12} + \mathcal{L}'_{13}\xi) X_L^T J_L^N - \frac{T_R}{\mathcal{L}'_{11}} J_L^{N^2}. \quad (15)$$

We notice that the nonlinear term in Eq. (13) does not contribute to the output power and it only depends on J_L^N (or X_L^μ) at fixed X_L^T and X_P^T .

From the energy conservation law, the output power of the heat engine is equal to the sum of all the heat currents exchanged between the system and the three reservoirs i.e., $P = J_L^Q + J_P^Q + J_R^Q$, where J_R^Q is the heat current from the right reservoir. We can express all the heat currents in terms of J_L^N as follows:

$$J_L^Q = \left[\left(\frac{\mathcal{L}'_{11}\mathcal{L}'_{22} - \mathcal{L}'_{21}\mathcal{L}'_{12}}{\mathcal{L}'_{11}} \right) + \left(\frac{\mathcal{L}'_{11}\mathcal{L}'_{23} - \mathcal{L}'_{21}\mathcal{L}'_{13}}{\mathcal{L}'_{11}} \right) \xi \right] X_L^T + \frac{\mathcal{L}'_{21}}{\mathcal{L}'_{11}} J_L^N - \gamma_h J_L^{N^2}, \quad (16)$$

$$J_P^Q = \left[\left(\frac{\mathcal{L}'_{11}\mathcal{L}'_{32} - \mathcal{L}'_{31}\mathcal{L}'_{12}}{\mathcal{L}'_{11}} \right) + \left(\frac{\mathcal{L}'_{11}\mathcal{L}'_{33} - \mathcal{L}'_{31}\mathcal{L}'_{13}}{\mathcal{L}'_{11}} \right) \xi \right] X_L^T + \frac{\mathcal{L}'_{31}}{\mathcal{L}'_{11}} J_L^N, \quad (17)$$

$$J_R^Q = \left[\frac{(\mathcal{L}'_{12} + \mathcal{L}'_{13}\xi)(\mathcal{L}'_{21} + \mathcal{L}'_{31})}{\mathcal{L}'_{11}} - (\mathcal{L}'_{22} + \mathcal{L}'_{32} + (\mathcal{L}'_{23} + \mathcal{L}'_{33})\xi) \right] X_L^T + \left[\frac{T_R}{\mathcal{L}'_{11}} (\mathcal{L}'_{12} + \mathcal{L}'_{13}\xi) X_L^T - \frac{(\mathcal{L}'_{21} + \mathcal{L}'_{31})}{\mathcal{L}'_{11}} \right] J_L^N - \gamma_c J_L^{N^2}, \quad (18)$$

where γ_c denotes the strength of dissipation to the cold reservoir (right) which is defined as

$$\gamma_c = \frac{T_R}{\mathcal{L}'_{11}} - \gamma_h > 0. \quad (19)$$

Let us define a dimensionless parameter representing dissipation strength ratio, $\alpha = 1/(1 + \gamma_c/\gamma_h)$. The asymmetry dissipation limits $\gamma_c/\gamma_h \rightarrow \infty$ (i.e., $\gamma_h \rightarrow 0$) and $\gamma_c/\gamma_h \rightarrow 0$ (i.e., $\gamma_c \rightarrow 0$) corresponds to $\alpha = 0$ and $\alpha = 1$, respectively and by setting $\alpha = 0$ we will recover the linear-response results.

The efficiency of a three-terminal heat engine operating between the temperatures $T_R < T_P < T_L$ at a given output power is defined as

$$\eta = \frac{P}{\sum_{\nu+} J_\nu^Q} = \frac{-T X_L^V J_L^N}{\sum_{\nu+} J_\nu^Q}, \quad (20)$$

where $\sum_{\alpha+} J_\alpha^Q$ represents only positive heat currents ($J_\nu^Q > 0$) absorbed by the system from the reservoir. We consider $J_R^Q < 0$ and $J_L^Q > 0$ for our system to work as a heat engine. Depending on the sign of J_P^Q , the efficiency of the voltage probe heat engine when only $J_L^Q > 0$ is given by

$$\eta_L = \frac{P}{J_L^Q}, \quad (21)$$

or when both $J_L^Q > 0$ and $J_P^Q > 0$,

$$\eta_{LP} = \frac{P}{J_L^Q + J_P^Q}. \quad (22)$$

We refer to the efficiency of the voltage probe heat engine as η_m with index $m = L, LP$.

1. Efficiency at maximum output power

We now derive the maximum output power and its corresponding efficiency by taking the derivative of the output power and setting $\partial P/\partial J_L^N = 0$. Then,

$$J_L^{N*} = (\mathcal{L}'_{12} + \mathcal{L}'_{13}\xi) \frac{X_L^T}{2}, \quad X_L^{\mu*} = \frac{-(\mathcal{L}'_{12} + \mathcal{L}'_{13}\xi) X_L^T}{2\mathcal{L}'_{11}}. \quad (23)$$

Substituting the value of J_L^{N*} in Eq. (15), the maximum output power can be expressed as

$$P_{max} = \frac{T}{4\mathcal{L}'_{11}} (\mathcal{L}'_{12} + \mathcal{L}'_{13}\xi)^2 X_L^{T^2}, \quad (24)$$

$$= \frac{T^4}{4} G_{LL}(\phi) [S_{LL}(\phi) + S_{LP}(\phi)\xi]^2 X_L^{T^2},$$

where $G_{LL}(\phi)$ is the electrical conductance, $S_{LL}(\phi)$ and $S_{LP}(\phi)$ are the Seebeck coefficients for the voltage probe

heat engine defined in Eq. (B5) and Eq. (B2) in Appendix B. Also, we use $(\mu_R, T_R) = (\mu, T)$ as the reference.

Using Eqs. (23) and (24) in the efficiency expression defined in Eqs. (21) and (22), the efficiency at maximum power is derived as follows:

$$\eta_m(P_{max}) = \eta_{C,m}(P_{max}) \frac{x_m y_m}{2(y_m + 2d_m) - \alpha T X_L^T x_m y_m}, \quad (25)$$

where $\eta_{C,m}(P_{max})$ is the value of the Carnot efficiency derived by substituting $X_L^\mu = X_L^{\mu*}$ in Eq. (C1) and Eq. (C2). The Carnot efficiency for a three-terminal heat engine is discussed in Appendix C. We introduce the asymmetry parameter x_m in the expression of efficiency at maximum output power and it is defined as [55]

$$x_m = \frac{r_m}{y_m}, \quad (26)$$

where

$$r_m = (2\delta Z_m^A + Z_m^B + \delta^2 Z_m^C)T. \quad (27)$$

The generalized figure of merit y_m for the voltage probe heat engine is expressed as [55]

$$y_m = [\delta(Z_m^A + Z_m^{A'}) + Z_m^B + \delta^2 Z_m^C]T, \quad (28)$$

where $\delta = 1/\xi$ and the term $Z_m^\theta T$ with $\theta = A, A', A'', B, B', C, C'$ are given in Eq. (B10) of Appendix B. The time-reversal symmetry case refers to $x_m = 1$.

The parameter d_m in Eq. (25) is related to the thermal conductance and temperature bias ratio of the system [55] and it is defined as

$$\begin{aligned} d_L &= \delta \frac{K_{PL} + K_{LP}}{K_{LL}} + \frac{K_{PP}}{K_{LL}} + \delta^2 \quad \text{if } J_L^Q > 0, \\ d_{LP} &= \frac{\delta K_{PL} + K_{PP}}{K_{LP}} + \delta^2 \frac{K_{LL}}{K_{LP}} + \delta \quad \text{if } J_L^Q, J_P^Q > 0. \end{aligned} \quad (29)$$

Here K_{ij} are thermal conductance terms defined in Eq. (B8) of Appendix B.

2. Efficiency at a given output power

The optimal performance of our minimally nonlinear voltage probe heat engine can be examined by defining the relative power gain ΔP as

$$\Delta P = \frac{P - P_{max}}{P_{max}}, \quad (30)$$

where $-1 \leq \Delta P \leq 0$. After simplicity, the relative power can be written as

$$\frac{P}{P_{max}} = 1 + \Delta P = \frac{J_L^N X_L^\mu}{J_L^{N*} X_L^{\mu*}} = \chi(2 - \chi), \quad (31)$$

where $\chi = X_L^\mu / X_L^{\mu*}$. The normalized efficiency for the voltage probe heat engine can be calculated as follows:

$$\frac{\eta_m}{\eta_m(P_{max})} = \frac{\eta_{C,m}}{\eta_{C,m}(P_{max})} \frac{\chi(2 - \chi) [2(y_m + 2d_m) - \alpha T X_L^T x_m y_m]}{4(y_m + d_m) - 2y_m \chi - \alpha T X_L^T (2 - \chi)^2 x_m y_m}. \quad (32)$$

The efficiency at a given output power can be expressed as

$$\eta_m = \eta_{C,m} \frac{\chi(2 - \chi) x_m y_m}{4(y_m + d_m) - 2y_m \chi - \alpha T X_L^T (2 - \chi)^2 x_m y_m}. \quad (33)$$

The dependency of the efficiency at a given output power on the power gain can further be obtained by solving Eq. (31) as

$$\chi_{\pm} = 1 \pm \sqrt{-\Delta P}. \quad (34)$$

Here, the plus (minus) sign refers to the favorable (unfavorable) branch. As we increase the voltage bias, the normalized efficiency goes beyond P/P_{max} for the favorable branch.

The normalized efficiency and the efficiency at a given output power are expressed in terms of the relative power gain ΔP as follows:

$$\frac{\eta_m}{\eta_m(P_{max})} = \frac{\eta_C}{\eta_C(P_{max})} \frac{(1 + \Delta P) [2(y_m + 2d_m) - \alpha T X_L^T x_m y_m]}{4(y_m + d_m) - 2y_m (1 \pm \sqrt{-\Delta P}) - \alpha T X_L^T [2 - (1 \pm \sqrt{-\Delta P})]^2 x_m y_m}, \quad (35)$$

$$\eta_m = \eta_{C,m} \frac{(1 + \Delta P)x_m y_m}{4(y_m + d_m) - 2y_m(1 \pm \sqrt{-\Delta P}) - \alpha T X_L^T [2 - (1 \pm \sqrt{-\Delta P})]^2 x_m y_m}. \quad (36)$$

3. Upper bound on efficiency at maximum output power

The asymmetry parameter x_m is a measure of the asymmetry of the off-diagonal elements of the Onsager matrix by breaking the time-reversal symmetry in the presence of a nonzero magnetic field. Although there is no constraint on x_m , the generalized figure of merit y_m is bounded from above due to the bounds on the Onsager coefficients defined in Eq. (10). For the voltage probe heat engine, the third inequality in Eq. (10) can be expressed in terms x_m and y_m as follows:

$$\begin{aligned} H_m &\leq y_m \leq 0 \quad \text{for } d_m x_m \leq 0, \\ H_m &\geq y_m \geq 0 \quad \text{for } d_m x_m \geq 0, \end{aligned} \quad (37)$$

where the bound function H_m is defined as [55]

$$H_m = \frac{d_m x_m}{(x_m - 1)^2}. \quad (38)$$

Equation (38) shows that the sign of y_m is associated with the sign of both x_m and d_m .

By setting $y_m = H_m$ in Eq. (25), we can obtain the upper bound on efficiency at maximum output power for a minimally nonlinear voltage probe heat engine as follows:

$$\eta_m^*(P_{max}) = \frac{\eta_{C,m}(P_{max})x_m^2}{2(2x_m^2 - 3x_m + 2) - \alpha T X_L^T x_m^2}. \quad (39)$$

Equation (39) is a universal upper bound on the efficiency at maximum power for a minimally nonlinear voltage probe heat engine with broken time-reversal symmetry.

For the time-reversal symmetry case, i.e., $x_m = 1$, the above upper bound reduces to

$$\eta_m^*(P_{max}) = \frac{\eta_{C,m}(P_{max})}{2 - \alpha T X_L^T}. \quad (40)$$

For $0 \leq \alpha \leq 1$ and $x_m = 1$, $\eta_m^*(P_{max})$ can take values between

$$\frac{\eta_{C,m}(P_{max})}{2} \leq \eta_m^*(P_{max}) \leq \frac{\eta_{C,m}(P_{max})}{2 - T X_L^T}. \quad (41)$$

We observe from Eq. (41) that the upper bound on the efficiency at maximum output power is enhanced and can exceed the CA limit by introducing nonlinearity into the system.

B. Voltage-temperature probe heat engine

For a minimally nonlinear voltage-temperature probe heat engine, the extended Onsager relation for the particle current and the heat current from the left reservoir

are expressed as follows:

$$\begin{aligned} J_L^N &= \mathcal{L}_{11}'' X_L^\mu + \mathcal{L}_{12}'' X_L^T, \\ J_L^Q &= \mathcal{L}_{21}'' X_L^\mu + \mathcal{L}_{22}'' X_L^T - \gamma_h J_L^{N^2}, \end{aligned} \quad (42)$$

where $-\gamma_h J_L^{N^2}$ denotes the dissipation to the hot reservoir and $\gamma_h > 0$ indicates the dissipation strength. By choosing J_L^N as our control parameter at a fixed value of X_L^T , we can write

$$X_L^\mu = \frac{J_L^N - \mathcal{L}_{12}'' X_L^T}{\mathcal{L}_{11}''}. \quad (43)$$

The output power $P = -T_R X_L^\mu J_L^N > 0$ for the voltage-temperature probe heat engine is given by

$$P = \frac{\mathcal{L}_{12}'' T_R X_L^T}{\mathcal{L}_{11}''} J_L^N - \frac{T_R}{\mathcal{L}_{11}''} J_L^{N^2}, \quad (44)$$

Following the energy conservation law, the heat current to the right (cold) reservoir is given by $J_R^Q = P - J_L^Q$. We can write the heat currents in terms of J_L^N as follows:

$$\begin{aligned} J_L^Q &= \left(\frac{\mathcal{L}_{11}'' \mathcal{L}_{22}'' - \mathcal{L}_{12}'' \mathcal{L}_{21}''}{\mathcal{L}_{11}''} \right) X_L^T + \frac{\mathcal{L}_{21}''}{\mathcal{L}_{11}''} J_L^N - \gamma_h J_L^{N^2}, \\ J_R^Q &= \left(\frac{\mathcal{L}_{12}'' \mathcal{L}_{21}'' - \mathcal{L}_{11}'' \mathcal{L}_{22}''}{\mathcal{L}_{11}''} \right) X_L^T + \left(\frac{\mathcal{L}_{12}'' \eta_C - \mathcal{L}_{21}''}{\mathcal{L}_{11}''} \right) J_L^N \\ &\quad - \gamma_c J_L^{N^2}. \end{aligned} \quad (45)$$

Here $\gamma_c = T_R/\mathcal{L}_{11}'' - \gamma_h > 0$ is dissipation strength to the cold reservoir. Like the voltage probe case, we define the dimensionless parameter denoting dissipation strength ratio, $\alpha = 1/(1 + \gamma_c/\gamma_h)$, where it takes values from $0 \leq \alpha \leq 1$ for asymmetric dissipation limits $\gamma_c/\gamma_h \rightarrow \infty$ and $\gamma_c/\gamma_h \rightarrow 0$. Linear Onsager relations are obtained by taking $\alpha = 0$.

The efficiency at a given output power, $\eta = \frac{P}{J_L^Q}$ with $J_L^Q > 0$ is defined as

$$\eta = \frac{\mathcal{L}_{12}'' \eta_C J_L^N - T_R J_L^{N^2}}{(\mathcal{L}_{11}'' \mathcal{L}_{22}'' - \mathcal{L}_{12}'' \mathcal{L}_{21}'') X_L^T + \mathcal{L}_{12}'' J_L^N - \alpha T_R J_L^{N^2}}. \quad (47)$$

1. Efficiency at maximum output power

The maximum output power for a voltage-temperature probe heat engine can be obtained by taking the derivative of output power in Eq. (44) with J_L^N to be zero i.e., $\partial P/\partial J_L^N = 0$. This implies

$$J_L^{N*} = \frac{\mathcal{L}_{12}'' X_L^T}{2}, \quad X_L^{\mu*} = -\frac{\mathcal{L}_{12}'' X_L^T}{2\mathcal{L}_{11}''}. \quad (48)$$

The maximum output power is obtained by substituting J_L^{N*} in Eq. (44) and it is expressed as follows:

$$P_{max} = \frac{T\mathcal{L}_{12}''^2}{4\mathcal{L}_{11}''} X_L^{T2} = \frac{T^4}{4} G_{LL}(\phi) S_{LL}(\phi)^2 X_L^{T2}, \quad (49)$$

where $G_{LL}(\phi)$ and $S_{LL}(\phi)$ are the electrical conductance and Seebeck coefficients for the voltage-temperature probe heat engine, respectively (see Eq. (B6) and Eq. (B3) in Appendix B.

The efficiency at maximum output power is derived as follows:

$$\eta(P_{max}) = \eta_C \frac{xy}{2(y+2) - \alpha T X_L^T xy}, \quad (50)$$

where $\eta_C = 1 - T_R/T_L (= T_R X_L^T)$ is the Carnot efficiency for the voltage-temperature probe heat engine. The asymmetry parameter x and the generalized figure of merit y for the voltage-temperature probe heat engine are defined as follows:

$$x = \frac{S_{LL}(\phi)}{S_{LL}(-\phi)}, \quad (51)$$

$$y = \frac{G_{LL}(\phi) S_{LL}(\phi) S_{LL}(-\phi) T}{K_{LL}}. \quad (52)$$

Here, $S_{LL}(-\phi)$ and the thermal conductance, K_{LL} for the voltage-temperature probe heat engine are defined in Eq. (B3) and Eq. (B9) in Appendix B, respectively.

2. Efficiency at a given output power

The performance of the minimally nonlinear voltage-temperature heat engine can be optimized by defining

$$\frac{\eta}{\eta(P_{max})} = \frac{(1 + \Delta P)[2(y+2) - \alpha T X_L^T xy]}{4(y+1) - 2y(1 \pm \sqrt{-\Delta P}) - \alpha T X_L^T (2 - (1 \pm \sqrt{-\Delta P}))^2 xy}, \quad (58)$$

$$\eta = \eta_C \frac{(1 + \Delta P)xy}{4(y+1) - 2y(1 \pm \sqrt{-\Delta P}) - \alpha T X_L^T (2 - (1 \pm \sqrt{-\Delta P}))^2 xy}. \quad (59)$$

3. Upper bound on efficiency at maximum output power

The generalized figure of merit y for the voltage-temperature probe heat engine is bounded due to the constraints on the Onsager coefficients as discussed in Eq. (12) and it is expressed as follows:

$$\begin{aligned} H &\leq y \leq 0 \quad \text{for } x \leq 0, \\ H &\geq y \geq 0 \quad \text{for } x \geq 0, \end{aligned} \quad (60)$$

the relative power gain ΔP as

$$\Delta P = \frac{P - P_{max}}{P_{max}}, \quad (53)$$

where $-1 \leq \Delta P \leq 0$. Following from the above definition, the relative power can be written as

$$\frac{P}{P_{max}} = 1 + \Delta P = \frac{-T X_L^\mu J_L^N}{-T X_L^{\mu*} J_L^{N*}} = \chi(2 - \chi), \quad (54)$$

where $\chi = X_L^\mu / X_L^{\mu*}$. The normalized efficiency can be derived as

$$\frac{\eta}{\eta(P_{max})} = \chi(2 - \chi) \frac{2(y+2) - \alpha T X_L^T xy}{4(y+1) - 2y\chi - \alpha T X_L^T (2 - \chi)^2 xy}, \quad (55)$$

and the efficiency at a given output power can be expressed as

$$\eta = \eta_C \frac{\chi(2 - \chi)xy}{4(y+1) - 2y\chi - \alpha T X_L^T (2 - \chi)^2 xy}. \quad (56)$$

Further, by solving Eq. (54), we can write

$$\chi_{\pm} = 1 \pm \sqrt{-\Delta P}, \quad (57)$$

where χ_+ is called the favorable branch and χ_- is called the unfavorable branch.

The normalized efficiency and the efficiency at a given output power as a function of power gain ΔP for a voltage-temperature probe heat engine are expressed as follows:

where the bound function H for the voltage-temperature probe heat engine is defined as

$$H = \frac{x}{(x-1)^2}. \quad (61)$$

By setting $y = H(x)$ in Eq. (50), we can obtain the upper bound on efficiency at maximum output power for

a voltage-temperature probe heat engine as follows:

$$\eta^*(P_{max}) = \eta_C \frac{x^2}{2(2x^2 - 3x + 2) - \alpha T X_L^T x^2}. \quad (62)$$

Equation (62) is a universal upper bound on the efficiency at maximum output power for a minimally nonlinear voltage-temperature probe heat engine with broken time-reversal symmetry.

For time-reversal symmetric case ($x = 1$), the above upper bound reduces to

$$\eta^*(P_{max}) = \frac{\eta_C}{2 - \alpha T X_L^T} = \frac{\eta_C}{2 - \alpha \eta_C}. \quad (63)$$

For $0 \leq \alpha \leq 1$, we can write

$$\frac{\eta_C}{2} \leq \eta^*(P_{max}) \leq \frac{\eta_C}{2 - \eta_C}. \quad (64)$$

Similar upper bounds on efficiency at maximum output power are also obtained for a two-terminal system with time-reversal symmetry [60, 79, 80]. We find that the introduction of nonlinearity and the broken time-reversal symmetry helps to enhance the upper bound on efficiency at maximum output power, allowing one to overcome the CA efficiency described in the linear response regime.

IV. TRIPLE-DOT AB HEAT ENGINE

We consider a three-terminal setup of triple-quantum-dot AB interferometer [65, 81–83], as illustrated in Fig. 2 to investigate the theory developed in the previous sections numerically. Here three QDs are arranged in a triangular geometry with each dot located at the vertex of an equilateral triangle and interconnected through quantum tunneling. A magnetic flux Φ threading the triangular ring perpendicularly. Dots 1 and 3 are connected to two reservoirs termed left (L) and right (R), respectively maintained at different temperatures ($T_L > T_R$) and chemical potentials ($\mu_L < \mu_R$). A probe (P) is connected to dot 2 to introduce inelastic scattering mechanisms into the system. The probe parameters (T_P, μ_P) are adjusted to examine a voltage probe and a voltage-temperature probe for our setup. Here we do not consider the electron-electron interactions and the spin degrees of freedom for simplicity. Thus, we can describe each QD by a spin-less electronic level and disregard the Zeeman effect. The total Hamiltonian \hat{H} of the whole system is expressed as,

$$\hat{H} = \hat{H}_{TQD} + \hat{H}_B + \hat{H}_{TQD,B} + \hat{H}_P + \hat{H}_{TQD,P}, \quad (65)$$

where, \hat{H}_{TQD} is the subsystem Hamiltonian for the triple QD system, \hat{H}_B and \hat{H}_P represent the bath (reservoir) Hamiltonian, and the probe Hamiltonian, respectively. $\hat{H}_{TQD,B}$ and $\hat{H}_{TQD,P}$ are the Hamiltonian for the interaction of the triple-dot system with the bath and the

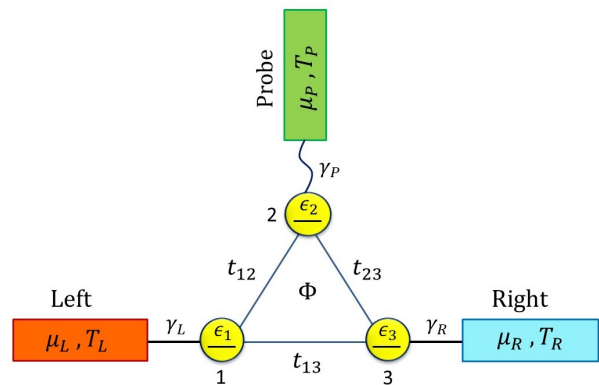


FIG. 2. Model of a three-terminal triple-dot AB heat engine consisting of three quantum dots arranged in a triangular geometry and a magnetic flux Φ pierces the triangular AB ring perpendicularly. Dot 1 and 3 are connected to two metallic leads (reservoirs) termed left (L) and right (R), respectively which are maintained at different temperatures and chemical potentials. Dot 2 is connected to a probe (P) that introduces inelastic scattering processes into the system. We set to $T_L > T_R$ and $\mu_L < \mu_R$ to ensure our system works as a thermoelectric heat engine. The probe parameters (T_P, μ_P) are adjusted to satisfy the condition for a voltage probe and voltage-temperature probe.

probe, respectively. We represent the individual Hamiltonian in the second quantization form. The subsystem Hamiltonian consisting of three interconnected dots is given as [65]

$$\hat{H}_{TQD} = \sum_{i=1,2,3} \epsilon_i \hat{d}_i^\dagger \hat{d}_i + \left[\sum_{i \neq j} t_{ij} \hat{d}_i^\dagger \hat{d}_j e^{i\phi_{ij}} + h.c. \right], \quad (66)$$

where, ϵ_i represents the energy of the i^{th} dot, \hat{d}_i^\dagger (\hat{d}_i) is the creation (annihilation) operator of the electrons in the i^{th} dot. The three quantum dots are connected by the inter-dot tunneling strength t_{ij} and ϕ_{ij} is the AB phase factor acquired by the electron wave while tunneling through the dots.

The Hamiltonian for the two reservoirs (leads) is given by

$$\hat{H}_B = \sum_{k, \nu \in L, R} \epsilon_{\nu, k} \hat{c}_{\nu, k}^\dagger \hat{c}_{\nu, k}. \quad (67)$$

Here $\epsilon_{\nu, k}$ is the energy of the k^{th} state in the reservoir ν and $\hat{c}_{\nu, k}^\dagger$ and $\hat{c}_{\nu, k}$ are the creation and annihilation operators of the electrons for the reservoirs.

The system-bath interaction Hamiltonian is represented as

$$\hat{H}_{TQD,B} = V_{1,L,k} \hat{d}_1^\dagger \hat{c}_{L,k} + V_{3,R,k} \hat{d}_3^\dagger \hat{c}_{R,k} + h.c.. \quad (68)$$

Here, $V_{1,L,k}$ and $V_{3,R,k}$ denote the interaction strength of the dot with the left (L) and the right (R) bath, respectively. Similarly, the probe Hamiltonian is given by

$$\hat{H}_P = \sum_k \epsilon_{P,k} \hat{c}_{P,k}^\dagger \hat{c}_{P,k}, \quad (69)$$

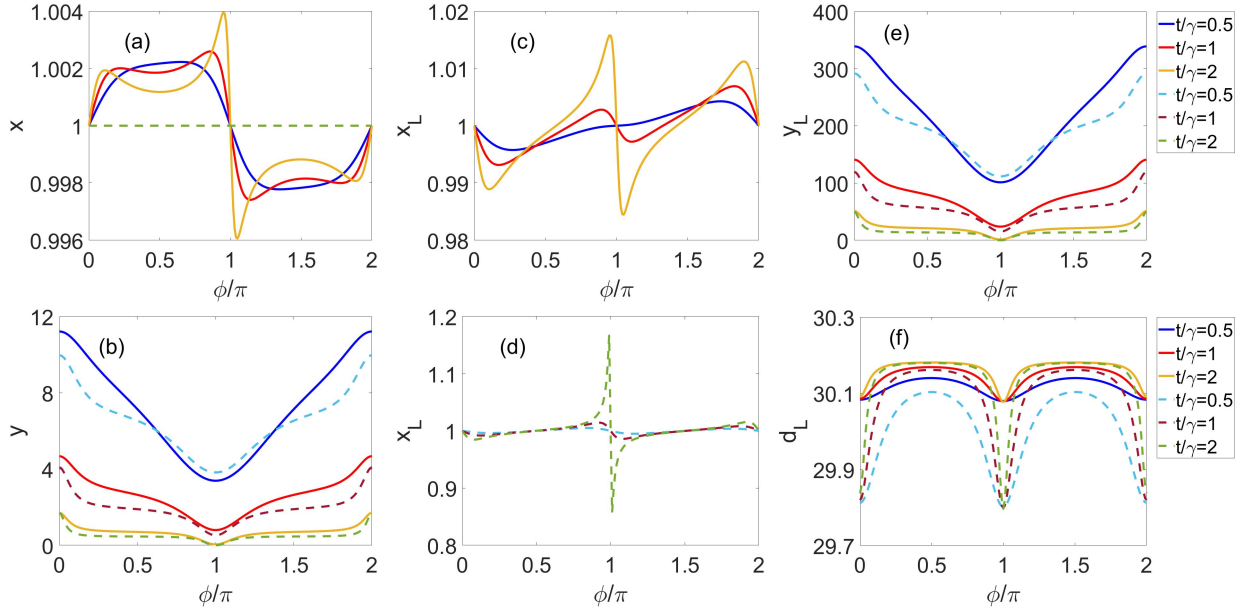


FIG. 3. (a) Asymmetry parameter x and (b) generalized figure of merit y as a function of ϕ for voltage-temperature probe heat engine; (c)-(d) asymmetry parameter x_L , (e) generalized figure of merit y_L , and (f) the parameter d_L as a function of ϕ in three different regimes of t/γ for voltage probe heat engine. Here solid lines represent non-degenerate dots, $\epsilon_1 \neq \epsilon_2 = \epsilon_3$ with $\epsilon_1 = 0.6$ and dashed lines represent degenerate dots, $\epsilon_1 = \epsilon_2 = \epsilon_3 = 0.5$. The parameters used are $\gamma_L = \gamma_R = \gamma = 0.1$, $\gamma_P = 0.005$, $\epsilon_2 = \epsilon_3 = 0.5$, $\mu_R = \mu = 0.3$, $T_R = T = 0.8$, $T_L = 1$, $T_P = 0.83$ (for voltage probe).

and the system-probe interaction Hamiltonian is given by

$$\hat{H}_{TQD,P} = V_{2,P,k} \hat{d}_2^\dagger \hat{c}_{P,k} + h.c. \quad (70)$$

Here, $\hat{c}_{P,k}^\dagger$ and $\hat{c}_{P,k}$ are the creation and annihilation operators of the electron in the k^{th} state of the probe, respectively. $V_{2,P,k}$ is the interaction strength between dot and the probe.

The AB phases ϕ_{ij} acquired by the electron's wave while tunneling through the dots satisfy the following relation [65, 76]:

$$\phi_{12} + \phi_{23} + \phi_{31} = \phi = 2\pi \frac{\Phi}{\Phi_0}, \quad (71)$$

where Φ is the total magnetic flux enclosed by the triangular AB ring and $\Phi_0 = h/e$ is the flux quantum. As the dots are at the vertices of an equilateral triangular loop and physical observables are gauge invariant in the steady-state, we may choose the gauge as $\phi_{12} = \phi_{23} = \phi_{31} = \phi/3$. We use the natural units convention $\hbar = c = e = k_B = 1$ for simplicity.

We use the Nonequilibrium Green's Function (NEGF) approach [84–86] to solve the model Hamiltonian and compute the observables. We solve the Heisenberg equation of motion for both the bath and the subsystem variables (see Ref. [65, 76, 87] for detailed calculations) and obtain the retarded $[G^+(\omega)]$ and advanced $[G^-(\omega)]$ Green's function for our system by using the quantum Langevin equation [87]. The retarded Green's function

which gives the dynamics of the electrons inside the system is defined as [65]

$$G^+(\omega) = [\omega I - H_{TQD} - \Sigma_L^+(\omega) - \Sigma_R^+(\omega) - \Sigma_P^+(\omega)]^{-1}, \quad (72)$$

where I is a (3×3) identity matrix and $\Sigma_\nu^+(\omega)$ is the self-energy of the reservoir $\nu = L, P, R$. For simplicity, we use the wide-band limit approximation where the real part of the self-energy vanishes when the density of states of the leads are energy independent and only the imaginary part of the self-energy exists which is given in terms of the hybridization matrix Γ_ν as $\Sigma_\nu^\pm = \mp i\Gamma_\nu/2$, where

$$\Gamma_{i,i'}^\nu = 2\pi \sum_k V_{i',k}^{\nu*} V_{i,k}^\nu \delta(\omega - \omega_k). \quad (73)$$

By setting $t_{ij} = t$, the retarded Green's function for the whole system can be expressed in the matrix form as

$$G^+(\omega) = \begin{pmatrix} \omega - \epsilon_1 + i\frac{\gamma_L}{2} & -te^{i\phi/3} & -te^{-i\phi/3} \\ -te^{-i\phi/3} & \omega - \epsilon_2 + i\frac{\gamma_P}{2} & -te^{i\phi/3} \\ -te^{i\phi/3} & -te^{-i\phi/3} & \omega - \epsilon_3 + i\frac{\gamma_R}{2} \end{pmatrix}^{-1}. \quad (74)$$

The hybridization matrices which account for the subsystem-bath coupling are given by

$$\Gamma^L = \begin{pmatrix} \gamma_L & 0 & 0 \\ 0 & 0 & 0 \\ 0 & 0 & 0 \end{pmatrix}, \Gamma^R = \begin{pmatrix} 0 & 0 & 0 \\ 0 & 0 & 0 \\ 0 & 0 & \gamma_R \end{pmatrix}, \Gamma^P = \begin{pmatrix} 0 & 0 & 0 \\ 0 & \gamma_P & 0 \\ 0 & 0 & 0 \end{pmatrix}, \quad (75)$$

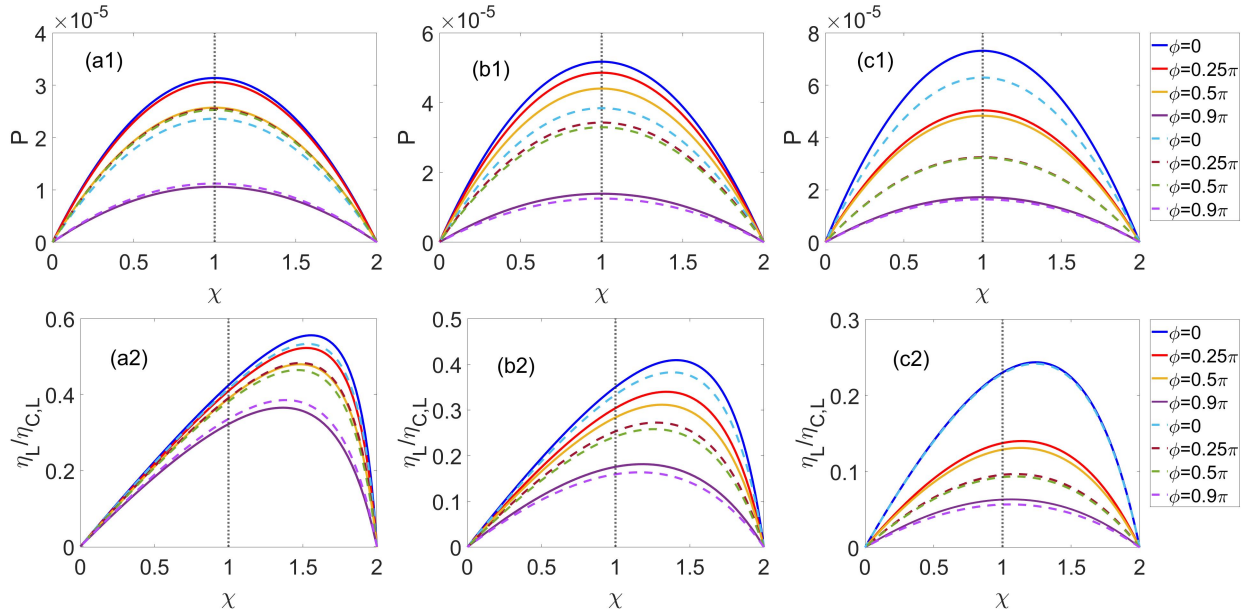


FIG. 4. Voltage probe heat engine: (a1)-(c1) output power, P and (a2)-(c2) efficiency at a given output power, $\eta_L/\eta_{C,L}$ as a function of χ for different values of ϕ . Three different regimes of t/γ are shown in (a1)-(a2) $t/\gamma = 0.5$, (b1)-(b2) $t/\gamma = 1$, and (c1)-(c2) $t/\gamma = 2$. The parameters used are $\epsilon_1 = 0.6$ (solid lines), $\epsilon_1 = 0.5$ (dashed lines), $\epsilon_2 = \epsilon_3 = 0.5$, $\gamma_L = \gamma_R = \gamma = 0.1$, $\gamma_P = 0.005$, $\mu_R = \mu = 0.3$, $T_R = T = 0.8$, $T_L = 1$, $T_P = 0.83$, $\alpha = 0$. The vertical dotted line shows the bias at maximum output power.

where γ_ν represents the dot-reservoir coupling strength.

The transmission of electrons from reservoir ν to λ terminal is defined by the transmission function as [88]:

$$T_{\nu\lambda} = Tr[\Gamma^\nu G^+ \Gamma^\lambda G^-]. \quad (76)$$

Here the advanced Green's function $G^-(\omega)$ is the conjugate transpose of the retarded Green's function $G^+(\omega)$.

The Landauer formula for the Particle current (J_ν^N) flowing from reservoir ν to the central system (with $\nu, \lambda = L, P, R$) is defined as [88–90]

$$J_\nu^N = \int_{-\infty}^{\infty} d\omega \left[\sum_{\lambda \neq \nu} T_{\nu\lambda}(\omega, \phi) f_\nu(\omega) - \sum_{\lambda \neq \nu} T_{\lambda\nu}(\omega, \phi) f_\lambda(\omega) \right]. \quad (77)$$

Similarly, the heat current (J_ν^Q) flowing from reservoir ν to the central system for arbitrary coupling is defined as [91–96]

$$J_\nu^Q = \int_{-\infty}^{\infty} d\omega (\omega - \mu_\nu) \left[\sum_{\lambda \neq \nu} T_{\nu\lambda}(\omega, \phi) f_\nu(\omega) - \sum_{\lambda \neq \nu} T_{\lambda\nu}(\omega, \phi) f_\lambda(\omega) \right], \quad (78)$$

where $f_\nu(\omega, \mu_\nu, T_\nu) = [\exp(\frac{\omega - \mu_\nu}{T_\nu}) + 1]^{-1}$ is Fermi-Dirac distribution function.

We can expand Eq. (77) and Eq. (78) up to linear order and write them in terms of Onsager relations as discussed in Eq. (3). With this background, we follow the theory developed in Sec. II and Sec. III and demonstrate the numerical results for a triple-dot AB heat engine in the following section.

V. RESULTS AND DISCUSSION

This section is dedicated to the discussion of numerical results for the theory developed in the previous sections. The thermoelectric performance of a voltage probe and a voltage-temperature probe heat engine is demonstrated by taking into account the broken time-reversal symmetry of the system in both linear response and minimally nonlinear regimes. We compare our results for two different setups of the system i.e., (i) non-degenerate dots $\epsilon_1 \neq \epsilon_2 = \epsilon_3$ and (ii) degenerate dots $\epsilon_1 = \epsilon_2 = \epsilon_3$ and also in three different regimes of t/γ ratio i.e., (a) $t/\gamma = 0.5$, (b) $t/\gamma = 1$, and $t/\gamma = 2$.

We observe that the efficiency of a voltage probe and voltage-temperature probe heat engine largely depends on the asymmetry parameter and the generalized figure of merits as discussed in Sec. III. Equation (56) shows that the efficiency of the voltage-temperature probe heat engine depends on the parameters x and y . However, the efficiency of the voltage probe heat engine, along with x_m and y_m , depends upon an additional parameter d_m (see Eq. (33)). Although the asymmetry parameters x , (x_m) are not restricted to taking any values, the generalized figure of merits y and (y_m) are bounded from above by the bound functions H and (H_m), respectively when the time-reversal symmetry is broken as discussed in Eq. (60) and Eq. (37). Firstly, to optimize the performance of the heat engine one needs to investigate these parameters with broken time-reversal symmetry in the presence of a nonzero magnetic field. We consider $J_L^Q > 0$ and

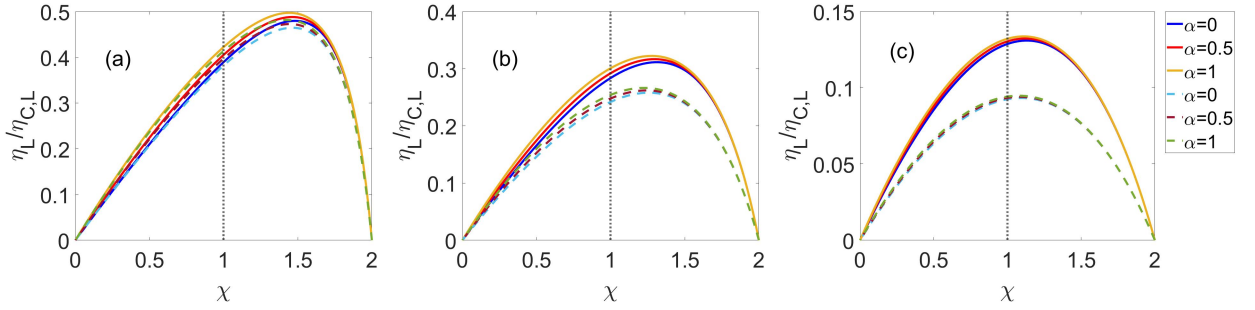


FIG. 5. Voltage probe heat engine: Efficiency at a given output power, $\eta_L/\eta_{C,L}$ as a function of χ at different dissipation strength α . Three different regimes of t/γ are shown in (a) $t/\gamma = 0.5$, (b) $t/\gamma = 1$, and (c) $t/\gamma = 2$. The parameters used are $\epsilon_1 = 0.6$ (solid lines), $\epsilon_1 = 0.5$ (dashed lines), $\epsilon_2 = \epsilon_3 = 0.5$, $\gamma_L = \gamma_R = \gamma = 0.1$, $\gamma_P = 0.005$, $\mu_R = \mu = 0.3$, $T_R = T = 0.8$, $T_L = 1$, $T_P = 0.83$, $\phi = 0.5\pi$. The vertical dotted line shows the bias at maximum output power.

$J_P^Q < 0$ to simulate the numerical results for the voltage probe heat engine.

Figure 3 shows the plots for x , y , x_L , y_L , and d_L as a function of ϕ (which is related to the magnetic flux given in Eq. (71)) in three different regimes of t/γ . Figure 3(a) illustrates that for a voltage-temperature probe heat engine, the time-reversal symmetry is broken ($x \neq 1$) for the non-degenerate dots (solid lines) setup. However, the time-reversal symmetry is preserved ($x = 1$) for the degenerate dots (dashed lines). Thus, to break the time-reversal symmetry, along with a non-vanishing magnetic field, we need some anisotropy in the system $\epsilon_1 \neq \epsilon_3$ for a voltage-temperature probe heat engine [48, 50]. However, the voltage probe heat engine shows time-reversal symmetry-breaking for both non-degenerate and degenerate dots with a large extent of asymmetry in degenerate dots case as shown in Fig. 3(c) and Fig. 3(d), respectively. The asymmetry due to the magnetic field is comparatively higher in the $t/\gamma = 2$ regime for both voltage probe and voltage-temperature probe heat engines. The generalized figure of merit y for the voltage-temperature probe in Fig. 3(b) and y_L for the voltage probe in Fig. 3(e) shows similar decreasing behavior as we increase ϕ from 0 to π then increases from π to 2π for both degenerate and non-degenerate dots. The values of y and y_L are higher for non-degenerate cases in all three regimes of t/γ with maximum value in the $t/\gamma = 0.5$ regime and minimum in the $t/\gamma = 2$ regime. Although y and y_L show similar behavior the magnitude of y_L is quite large as compared to y . The main difference between the voltage probe and voltage-temperature probe heat engine is the characteristic parameter d_m . Figure 3(f) shows the plot of d_L as a periodic function of ϕ with maximum value at $\phi = \pi/2$ and in $t/\gamma = 2$ regime. Degenerate dots show more variation with ϕ than the non-degenerate dots.

The performance of our voltage probe and voltage-temperature probe heat engines relies on the trade-off between the output power and the efficiency. We discuss the performance of the heat engines operating in the linear-response regime and in the minimally nonlinear regime where a dissipative second-order term ($-\gamma_h J_L^{N^2}$) is in-

troduced in the heat current from the left reservoir (J_L^Q) as shown in Eq. (13) and Eq. (42) for voltage probe and voltage-temperature probe heat engine, respectively. Figure 4 shows the plots for output power (P) and efficiency ($\eta_L/\eta_{C,L}$) as a function of relative bias χ at fixed values of ϕ for the voltage probe heat engine working in the linear response regime ($\alpha = 0$). The output power is a parabolic function of χ . In $t/\gamma = 0.5$ regime we obtain high output power at $\phi = 0$ and then the power decreases as we increase the value of ϕ for non-degenerate dots as shown in Fig. 4(a1). However, the degenerate dots' output power is maximum at $\phi = \pi/4$. In $t/\gamma = 1$ (see Fig. 4(b1)) and $t/\gamma = 2$ (see Fig. 4(c1)) regime, the maximum output power obtained at $\phi = 0$ and the power decreases by further increasing ϕ for both degenerate and non-degenerate dots. The efficiency at a given output power ($\eta_L/\eta_{C,L}$) increases monotonically as we increase the relative bias χ , and reach a maximum value that is higher than the efficiency at maximum power. Then the efficiency decreases as we further increase the bias as illustrated in Fig. 4(a2)-(c2). We observe that the efficiency is higher in the favorable branch (i.e., $\chi > 1$) as compared to the unfavorable branch (i.e., $\chi < 1$). The vertical dotted line marks the efficiency at maximum power and the efficiency at a given output power is higher at $\phi = 0$ and decreases by increasing ϕ in all the three regimes of t/γ for both degenerate and non-degenerate dots as shown in Fig. 4(a2)-(c2). Higher efficiency at $\phi = 0$ is owing to the higher value of the generalized figure of merit y_L as shown in Fig. 3(e). We observe that the output power is minimum in the $t/\gamma = 0.5$ regime and maximum in the $t/\gamma = 2$ regime. However, the efficiency shows the opposite trend, where the efficiency is maximum in $t/\gamma = 0.5$ and minimum in $t/\gamma = 2$ regime. The output power and efficiency in the $t/\gamma = 1$ regime lie in between the above two regimes. The output power and efficiency at a given power are higher for non-degenerate dots than the degenerate dots. We observe that there exists an optimal power-efficiency trade-off for the voltage probe heat engine. The most efficient heat engine operating at a slightly lower output power than the maximum output power is desirable for optimal performance. The

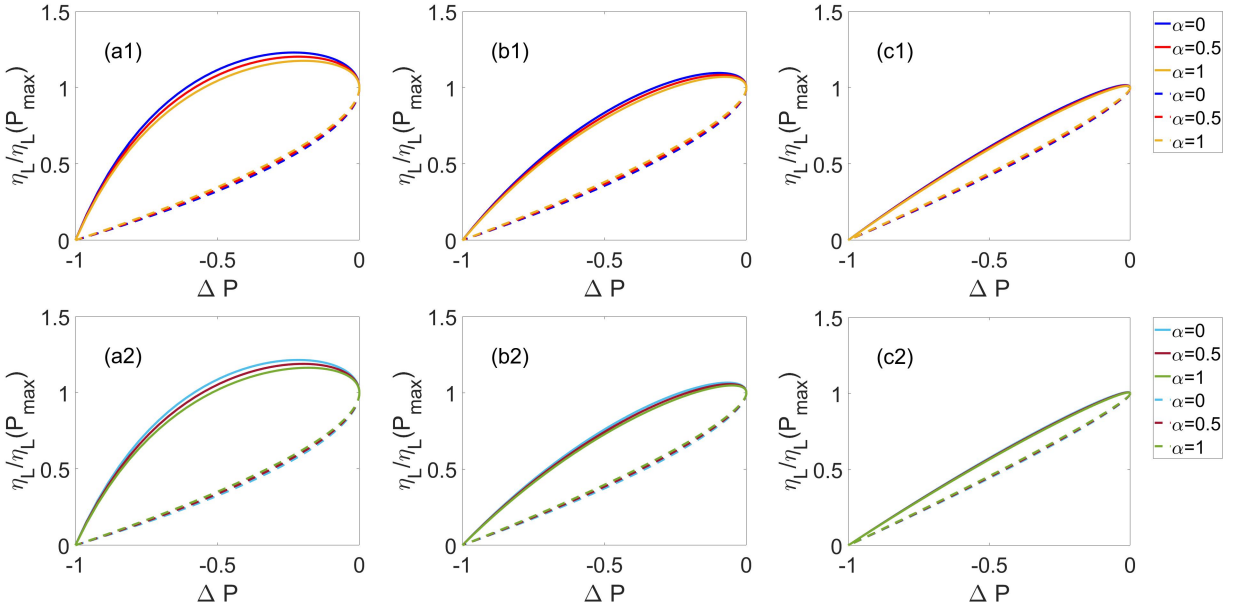


FIG. 6. Voltage probe heat engine: Normalized efficiency, $\eta_L/\eta_L(P_{max})$ as a function of power gain ΔP for favorable branch χ_+ (solid line) and unfavorable branch χ_- (dashed line) at different dissipation strength α . Three different regimes of t/γ are shown in (a1)-(a2) $t/\gamma = 0.5$, (b1)-(b2) $t/\gamma = 1$, and (c1)-(c2) $t/\gamma = 2$. (a1)-(c1) Non-degenerate dots, $\epsilon_1 \neq \epsilon_2 = \epsilon_3$ with $\epsilon_1 = 0.6$, (a2)-(c2) degenerate dots, $\epsilon_1 = \epsilon_2 = \epsilon_3 = 0.5$. The parameters used are $\epsilon_2 = \epsilon_3 = 0.5$, $\gamma_L = \gamma_R = \gamma = 0.1$, $\gamma_P = 0.005$, $\mu_R = \mu = 0.3$, $T_R = T = 0.8$, $T_L = 1$, $T_P = 0.83$, $\phi = 0.5\pi$.

choice of the t/γ regime depends on whether one needs a highly efficient heat engine with lower power or a low efficient engine that can generate high output power.

Figure 5 shows the plot for efficiency at a given power ($\eta_L/\eta_{C,L}$) as a function of χ at $\phi = \pi/2$ in the minimally nonlinear regime at different values of dissipation strength (α) for the voltage probe heat engine. We observe that the efficiency increases by increasing the dissipation strength α in all three regimes of t/γ for both degenerate and non-degenerate dots. However, for large biases, the increasing trend of efficiency vanishes and the efficiency is reduced for the higher extent of dissipation. To understand it properly we demonstrate the normalized efficiency ($\eta_L/\eta_L(P_{max})$) versus power gain (ΔP) plot in Fig. 6. For a given power gain, the normalized efficiency is reduced with increasing α in the favorable branch, χ_+ (solid lines), and the opposite happens in the unfavorable branch, χ_- (dashed lines) for both non-degenerate dots (Fig. 6(a1)-(c1)) and degenerate dots (Fig. 6(a2)-(c2)). We notice that at a fixed power gain, the voltage probe heat engine works more efficiently in the favorable branch and reach maximum efficiency than in the unfavorable branch for both degenerate and non-degenerate dots in all three regimes of t/γ . We observe that the power gain at maximum efficiency is relatively lower in the $t/\gamma = 0.5$ (Fig. 6(a1), (a2)) regime than the $t/\gamma = 1$ (Fig. 6(b1), (b2)) and $t/\gamma = 2$ (Fig. 6(c1), (c2)) regimes. The power gain at maximum efficiency and the efficiency at maximum power are relatively close in the $t/\gamma = 2$ regime as compared to the $t/\gamma = 1$ regime. In the $t/\gamma = 2$ regime, the power generated at maximum

efficiency is relatively close to maximum output power. However, the power generated at maximum efficiency is compromised and lower than the maximum output power in the $t/\gamma = 1$ regime and it is significantly reduced further in the $t/\gamma = 0.5$ regime.

Likewise, the voltage-temperature probe heat engine shows a similar behavior as the voltage probe heat engine. Since we are interested in breaking the time-reversal symmetry of the system, we consider only non-degenerate dots to study the power-efficiency trade-off. Figure 7 shows the output power and efficiency as a function of χ at fixed ϕ in the linear-response regime ($\alpha = 0$). We obtain maximum power and efficiency at $\phi = 0$ and the value reduces as we increase ϕ . We obtain minimum power with maximum efficiency in $t/\gamma = 0.5$ regime (see Fig. 7(a1)-(a2)). But, Fig. 7(c1)-(c2) shows the opposite trend for the $t/\gamma = 2$ regime where we get maximum power with minimum efficiency. The higher value of efficiency is related to the high value of the generalized figure of merit y at $\phi = 0$ in $t/\gamma = 0.5$ regime as shown in Fig. 3(b).

Figure 8 demonstrates the efficiency as a function of χ and normalized efficiency as a function of power gain ΔP in the minimally nonlinear regime at $\phi = \pi/2$ for the voltage-temperature probe heat engine. The maximum efficiency and the efficiency at maximum power rise as we increase the dissipation strength α in all three regimes of t/γ as shown in Fig. 8(a1)-(c1). Figure 8(a2)-(c2) shows that at a given power gain, the normalized efficiency is reduced by increasing the dissipation strength in the favorable branch. However, the opposite behav-

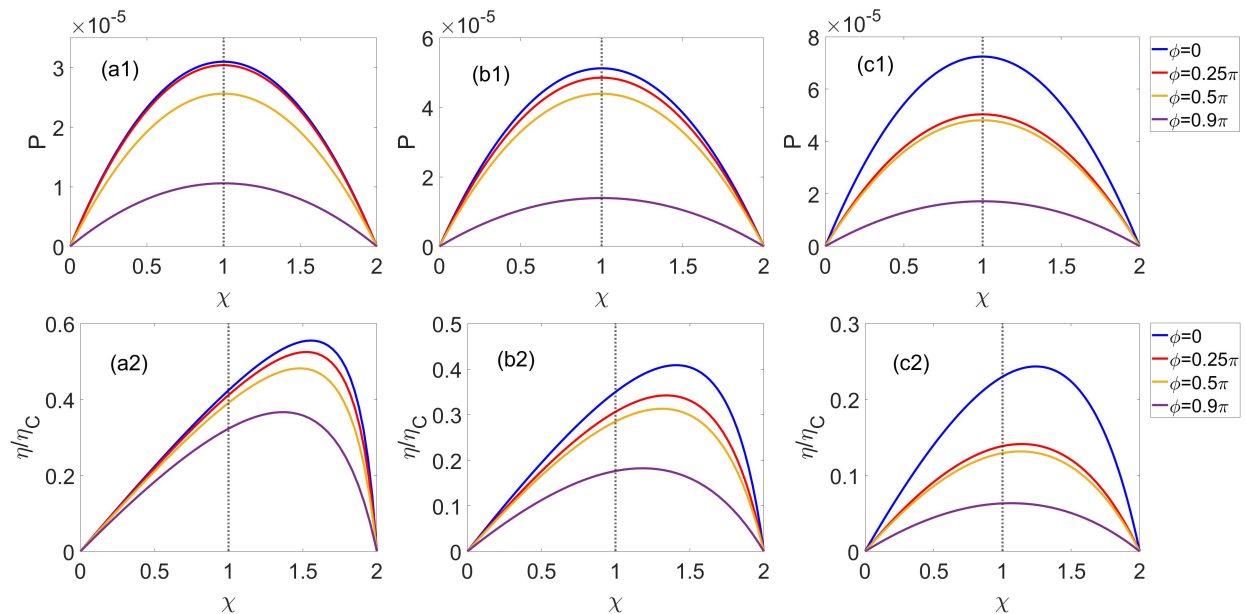


FIG. 7. Voltage-temperature probe heat engine: (a1)-(c1) output power, P and (a2)-(c2) efficiency at a given output power, η/η_C as a function of χ for different values of ϕ . Three different regimes of t/γ are shown in (a1)-(a2) $t/\gamma = 0.5$, (b1)-(b2) $t/\gamma = 1$, and (c1)-(c2) $t/\gamma = 2$. The parameters used are $\epsilon_1 = 0.6$, $\epsilon_2 = \epsilon_3 = 0.5$, $\gamma_L = \gamma_R = \gamma = 0.1$, $\gamma_P = 0.005$, $\mu_R = \mu = 0.3$, $T_R = T = 0.8$, $T_L = 1$, $\alpha = 0$. The vertical dotted line shows the bias at maximum output power.

ior is observed in the unfavorable branch where the normalized efficiency is enhanced with α . We can say that the dissipation effects introduced with nonlinearity are suppressed when we move toward higher voltage bias. Also, the normalized efficiency is higher in the favorable branch than in the unfavorable branch. Thus, at a given power gain, the voltage-temperature probe heat engine works more efficiently in the favorable branch than in the unfavorable branch. The efficiency at maximum output power is relatively close to the maximum efficiency in the $t/\gamma = 2$ regime. However, the power gain at maximum efficiency is lower than the maximum output power in the $t/\gamma = 1$ regime and it is further reduced significantly in the $t/\gamma = 0.5$ regime.

The CA limit, $\eta_{CA} = \eta_C/2$ is no longer an upper bound on the efficiency at maximum power with broken time-reversal symmetry [46–48, 50, 52, 55] and it can be exceeded in the nonlinear regime [56–60, 63, 64, 79, 80, 97–99]. With broken time-reversal symmetry, we derive a new upper bound on efficiency at maximum output power in Eq. (39) and Eq. (62) for minimally nonlinear voltage probe and voltage-temperature probe heat engine, respectively. Although the structure looks similar, their respective Carnot efficiencies and asymmetry parameters characterize the difference in the upper bounds obtained for the minimally nonlinear voltage probe and voltage-probe heat engine. Figure 9 shows the plot for the upper bound on efficiency at maximum output power within the context of broken time-reversal symmetry in the minimally nonlinear regime for voltage probe (Figure 9(a1)-(c1)) and voltage-temperature probe (Figure 9(a2)-(c2)) heat engine. The CA limit is exceeded with the bro-

ken time-reversal symmetry in the linear response regime ($\alpha = 0$). By increasing the dissipation strength α we can overcome the CA limit faster with broken time-reversal symmetry as well as with time-reversal symmetry.

We compare the performance of the voltage probe and voltage-temperature probe heat engine for a non-degenerate dots setup. There is not much difference in the output power and the efficiency of these two heat engines and the power-efficiency trade-off is very similar. The parameter d_L sets the main difference between voltage probe and voltage-temperature probe heat engine as shown in Eq. (33) and Eq. (56). We can write Eq. (33) in y_L/d_L form and we observe that the structure of Eq. (33) and Eq. (56) are exactly similar. Although we obtain large values of y_L and d_L for the voltage probe as shown in Fig. 3(e) and 3(f), the ratio y_L/d_L is equivalent to y . Because of this, the power-efficiency trade-off for both voltage probe and voltage-temperature probe heat engines is very much alike in all three regimes of t/γ for both linear and minimally nonlinear regimes.

VI. CONCLUSION

To conclude, we demonstrate the thermoelectric performance of a minimally nonlinear voltage probe and voltage-temperature probe heat engine for a general setup with broken time-reversal symmetry. The voltage probe and voltage-temperature probe successfully introduce dissipative and non-dissipative inelastic scattering mechanisms into the system, respectively. The probe parameters are adjusted to block the net particle current

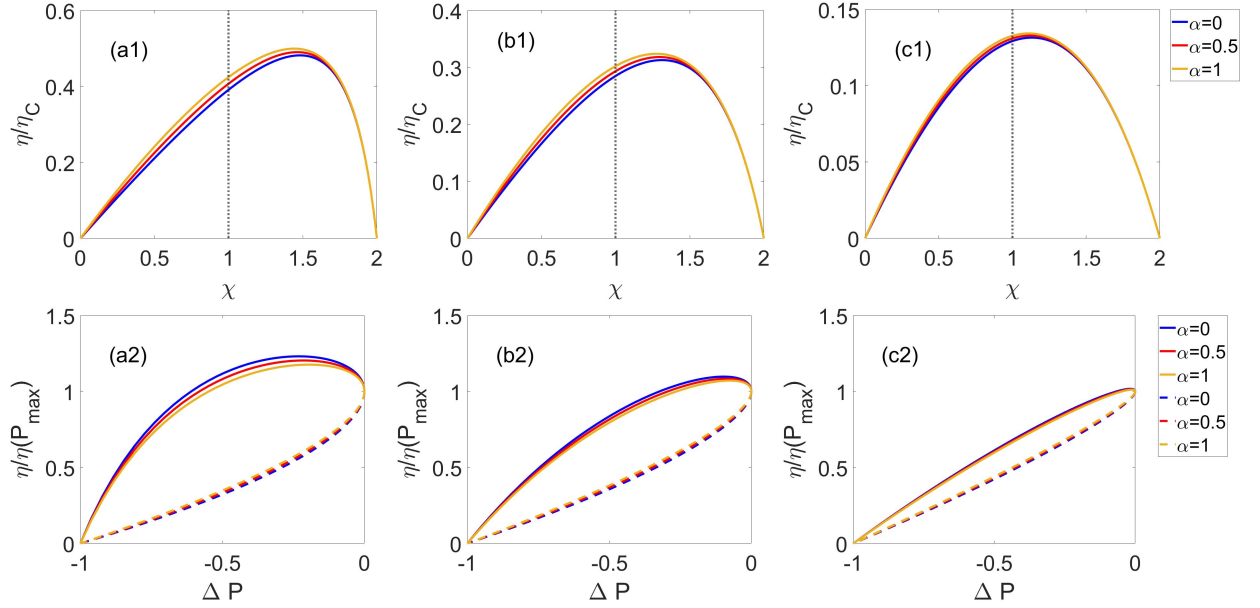


FIG. 8. Voltage-temperature probe heat engine: (a1)-(c1) efficiency at a given output power, η/η_C as a function of χ and (a2)-(c2) Normalized efficiency, $\eta/\eta(P_{max})$ as a function of power gain ΔP for favorable branch χ_+ (solid line) and unfavorable branch χ_- (dashed line) at different dissipation strength α . Three different regimes of t/γ are shown in (a1)-(a2) $t/\gamma = 0.5$, (b1)-(b2) $t/\gamma = 1$, and (c1)-(c2) $t/\gamma = 2$. The parameters used are $\epsilon_1 = 0.6$, $\epsilon_2 = \epsilon_3 = 0.5$, $\gamma_L = \gamma_R = \gamma = 0.1$, $\gamma_P = 0.005$, $\mu_R = \mu = 0.3$, $T_R = T = 0.8$, $T_L = 1$, $\alpha = 0$. The vertical dotted line shows the bias at maximum output power.

and only allow the heat current with the voltage probe, whereas both the particle and heat currents are blocked with the voltage-temperature probe. Our calculations are based on extended Onsager relations where a nonlinear term ($-\gamma_h J_L^{N^2}$) meaning power dissipation is introduced in the linear Onsager relation of the heat current. The nonlinear term can be seen as the inevitable power loss due to the finite time motion of the heat engine and this can be treated as a natural extension of linear irreversible thermodynamics. We derive the analytical expression for the efficiency at a given, the efficiency at maximum power, and the normalized efficiency in terms of asymmetric parameters (x, x_m), generalized figures of merit (y, y_m), d_m , and α for the voltage probe and voltage temperature probe heat engine. An additional parameter d_m is defined for the voltage probe heat engine can change the upper and lower bound on y_m . We define a dimensionless parameter α with $0 \leq \alpha \leq 1$, denoting the dissipation strength ratio which accounts for the nonlinearity in the system. We obtain a universal upper bound on the efficiency at maximum power for the voltage probe and voltage-temperature probe heat engines which exceeds the CA limit with nonlinearity as well as broken time-reversal symmetry.

We investigate a three-terminal triple-dot AB heat engine for numerical analysis of our results. We observe that in the presence of a nonzero magnetic field, unlike the voltage probe, the voltage-temperature probe heat engine required anisotropy in the system e.g., nondegenerate dots ($\epsilon_1 \neq \epsilon_3$) to break the time-reversal symmetry. We demonstrate the tunability of the system with t/γ

ratio. For both voltage probe and voltage-temperature probe heat engine, we obtain high efficiency but low output power when $t/\gamma < 1$, and the opposite trend happens when $t/\gamma > 1$. The higher efficiency in $t/\gamma < 1$ owing to the high value of the generalized figure of merit y_L and y for voltage probe and voltage-temperature probe heat engines, respectively. The controllability of t/γ ratio in a triple-dot AB interferometer is investigated experimentally in Ref. [100–104]. Both output power and efficiency are maximum in the time-reversal symmetry case ($x = 1$) at $\phi = 0$. The efficiency at a given power and the efficiency at maximum power are enhanced by increasing the dissipation strength although the output power remains unaffected. The normalized efficiency is higher and attains maximum efficiency at a power relatively smaller than the maximum power in the favorable branch. The normalized efficiency decreases by increasing the dissipation strength for the favorable branch but increases in the unfavorable branch. One can say the effects of dissipation are suppressed when we move towards higher voltage bias. Although we obtained high values for y_L and d_L , the value of the ratio $y_L/d_L \sim y$. Due to this reason, the power-efficiency trade-off for voltage probe and voltage-temperature probe heat engines are very similar. We obtain the upper bound on efficiency at maximum power for the minimally nonlinear voltage probe and voltage-temperature probe heat engines with broken time-reversal symmetry. The CA limit on efficiency at maximum power is exceeded with broken-time reversal symmetry and the introduction of nonlinearity makes it faster to overcome the CA limit even in the time-reversal

symmetry case. The difference in the upper bounds obtained for the voltage probe and the voltage-temperature heat engines are set by their respective Carnot efficiencies and asymmetry parameters. The upper bounds obtained in this paper are derived from the bounds on the Onsager coefficients using linear irreversible thermodynamics. We assume that the dissipation is weak. Hence, it is assumed that the bounds on the Onsager coefficients in the linear-response regime still hold for the minimally nonlinear heat engine. However, it would be interesting to investigate the extended Onsager relations containing higher-order nonlinear terms and evaluate the bounds on the extended Onsager coefficients satisfying the laws of thermodynamics.

ACKNOWLEDGEMENT

J.B. acknowledges the financial support received from IIT Bhubaneswar in the form of an Institute Research Fellowship. M.B. acknowledges support from the Anusandhan National Research Foundation (ANRF), India under MATRICS scheme Grant No. MTR/2021/000566. B.K.A. acknowledges CRG Grant No. CRG/2023/003377 from ANRF, Government of India. B.K.A. would like to acknowledge funding from the National Mission on Interdisciplinary Cyber-Physical Systems (NM-ICPS) of the Department of Science and Technology, Govt. of India through the I-HUB Quantum Technology Foundation, Pune, India.

Appendix A: Onsager coefficients

For a noninteracting system, the particle currents (J_ν^N) and the heat currents (J_ν^Q) from reservoir ν to λ (with $\nu, \lambda = L, P, R$) can be described using the Landauer-Buttiker formalism [88] as follows:

$$J_\nu^N = \int_{-\infty}^{\infty} d\omega \left[\sum_{\lambda \neq \nu} T_{\nu\lambda}(\omega, \phi) f_\nu(\omega) - \sum_{\lambda \neq \nu} T_{\lambda\nu}(\omega, \phi) f_\lambda(\omega) \right], \quad (\text{A1})$$

$$J_\nu^Q = \int_{-\infty}^{\infty} d\omega (\omega - \mu_\nu) \left[\sum_{\lambda \neq \nu} T_{\nu\lambda}(\omega, \phi) f_\nu(\omega) - \sum_{\lambda \neq \nu} T_{\lambda\nu}(\omega, \phi) f_\lambda(\omega) \right], \quad (\text{A2})$$

where $f_\nu(\omega, \mu_\nu, T_\nu) = [\exp(\frac{\omega - \mu_\nu}{T_\nu}) + 1]^{-1}$ is Fermi-Dirac distribution function and $T_{\nu\lambda}$ is the transmission probability from the ν to λ terminal.

The Onsager's coefficients are obtained by linearly expanding the currents J_ν^N and J_ν^Q defined in Eq. (77) and Eq. (78), respectively. The expression for Onsager

coefficients is given as follows:

$$\begin{aligned} \mathcal{L}_{11} &= T \int_{-\infty}^{\infty} d\omega (-\partial_\omega f)(T_{LR} + T_{LP}), \\ \mathcal{L}_{12} &= T \int_{-\infty}^{\infty} d\omega (-\partial_\omega f)(\omega - \mu)(T_{LR} + T_{LP}) = \mathcal{L}_{21}, \\ \mathcal{L}_{13} &= T \int_{-\infty}^{\infty} d\omega (-\partial_\omega f)(-T_{PL}), \\ \mathcal{L}_{14} &= T \int_{-\infty}^{\infty} d\omega (-\partial_\omega f)(\omega - \mu)(-T_{PL}) = \mathcal{L}_{23}, \\ \mathcal{L}_{22} &= T \int_{-\infty}^{\infty} d\omega (-\partial_\omega f)(\omega - \mu)^2(T_{LR} + T_{LP}), \\ \mathcal{L}_{24} &= T \int_{-\infty}^{\infty} d\omega (-\partial_\omega f)(\omega - \mu)^2(-T_{PL}), \\ \mathcal{L}_{31} &= T \int_{-\infty}^{\infty} d\omega (-\partial_\omega f)(-T_{LP}), \\ \mathcal{L}_{32} &= T \int_{-\infty}^{\infty} d\omega (-\partial_\omega f)(\omega - \mu)(-T_{LP}) = \mathcal{L}_{41}, \\ \mathcal{L}_{33} &= T \int_{-\infty}^{\infty} d\omega (-\partial_\omega f)(T_{PL} + T_{PR}), \\ \mathcal{L}_{34} &= T \int_{-\infty}^{\infty} d\omega (-\partial_\omega f)(\omega - \mu)(T_{PL} + T_{PR}) = \mathcal{L}_{43}, \\ \mathcal{L}_{42} &= T \int_{-\infty}^{\infty} d\omega (-\partial_\omega f)(\omega - \mu)^2(-T_{LP}), \\ \mathcal{L}_{44} &= T \int_{-\infty}^{\infty} d\omega (-\partial_\omega f)(\omega - \mu)^2(T_{PL} + T_{PR}). \end{aligned} \quad (\text{A3})$$

Here $(\partial_\omega f = -[4T \cosh^2(\frac{\omega - \mu}{2T})]^{-1})$ is the first-order derivative of the Fermi distribution function with energy.

Appendix B: Transport Coefficients

Transport coefficients, namely the Seebeck coefficient (S_{ij}), electrical conductance (G_{ij}), thermal conductance (K_{ij}), and Peltier coefficient (Π_{ij}) are the measures for the performance of a thermoelectric device. The local and nonlocal ($i \neq j$) transport coefficients are introduced in multiterminal systems that explain how the bias set between two reservoirs affects the transport between the other reservoirs [53, 55]. The relation between the transport coefficients and the Onsager coefficients is discussed in this section.

The Seebeck coefficient S_{ij} relates the voltage bias developed between the two reservoirs due to the temperature differences assuming zero net flow of particle current,

$$S_{ij} = - \frac{\Delta V_i}{\Delta T_j} \Bigg|_{(J_i^N=0 \forall \nu=i; \Delta T_\nu=0 \forall \nu \neq j)}, \quad (\text{B1})$$

where $\Delta V_i = \Delta \mu_i / e$. The local and nonlocal Seebeck coefficients for a voltage probe heat engine are given as

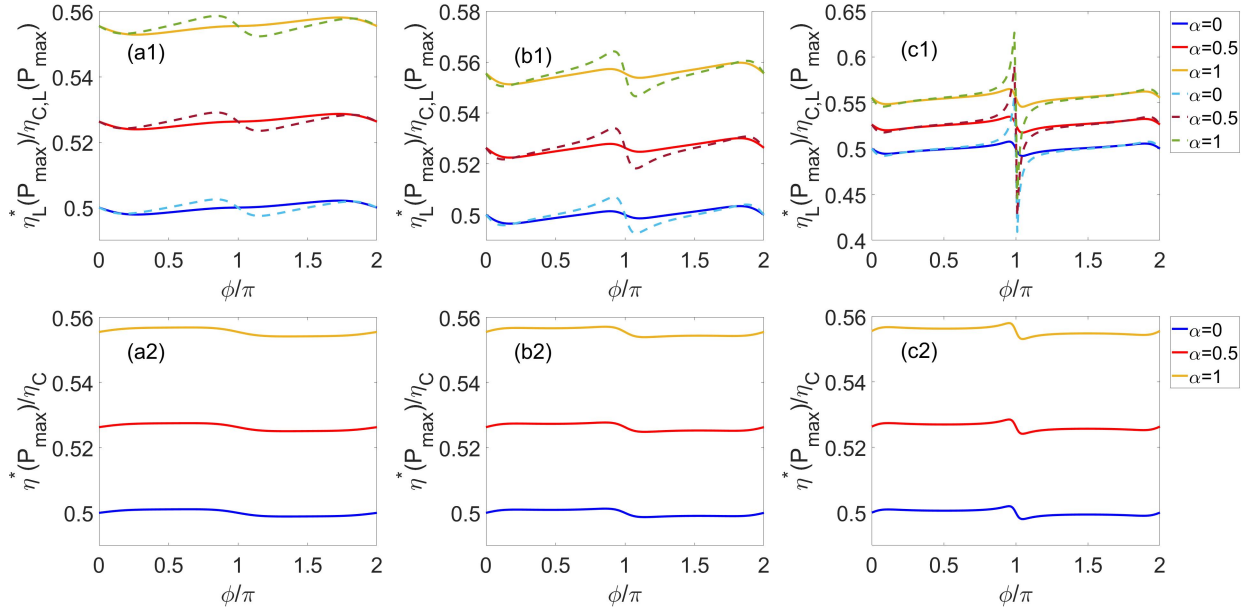


FIG. 9. Upper bound on efficiency at maximum power for (a1)-(c1) voltage probe and (a2)-(c2) voltage-temperature probe heat engine as a function ϕ at different dissipation strength α . Three different regimes of t/γ are shown in (a) $t/\gamma = 0.5$, (b) $t/\gamma = 1$, and (c) $t/\gamma = 2$. The parameters used are $\epsilon_1 = 0.6$, $\epsilon_2 = \epsilon_3 = 0.5$, $\gamma_L = \gamma_R = \gamma = 0.1$, $\gamma_P = 0.005$, $\mu_R = \mu = 0.3$, $T_R = T = 0.8$, $T_L = 1$, $T_P = 0.83$ (for voltage probe).

follows:

$$\begin{aligned} S_{LL}(\phi) &= \frac{\mathcal{L}'_{12}}{T\mathcal{L}'_{11}}, \quad S_{LP}(\phi) = \frac{\mathcal{L}'_{13}}{T\mathcal{L}'_{11}}, \\ S_{LL}(-\phi) &= \frac{\mathcal{L}'_{21}}{T\mathcal{L}'_{11}}, \quad S_{LP}(-\phi) = \frac{\mathcal{L}'_{31}}{T\mathcal{L}'_{11}}. \end{aligned} \quad (\text{B2})$$

Similarly, for a voltage-temperature probe heat engine, the Seebeck coefficient is defined as

$$S_{LL}(\phi) = \frac{\mathcal{L}''_{12}}{T\mathcal{L}''_{11}}, \quad S_{LL}(-\phi) = \frac{\mathcal{L}''_{21}}{T\mathcal{L}''_{11}}. \quad (\text{B3})$$

The electrical conductance describes the electric current dependency on the voltage bias between the reservoirs which is defined for a multiterminal setup as

$$G_{ij} = -\frac{J_i^N}{\Delta V_j} \Big|_{(\Delta V_\nu = 0 \forall \nu \neq j; \Delta T_\nu = 0 \forall \nu = i)}. \quad (\text{B4})$$

The electrical conductance for the voltage probe heat engine is defined as

$$G_{LL} = \frac{\mathcal{L}'_{11}}{T}, \quad (\text{B5})$$

and for the voltage-temperature probe heat engine, the electrical conductance is given as

$$G_{LL} = \frac{\mathcal{L}''_{11}}{T}. \quad (\text{B6})$$

The thermal conductance K_{ij} for a multiterminal setup explains the heat current dependency on the temperature

differences between the reservoirs,

$$K_{ij} = -\frac{J_i^Q}{\Delta T_j} \Big|_{(J_\nu^N = 0 \forall \nu = i; \Delta T_\nu = 0 \forall \nu \neq j)}. \quad (\text{B7})$$

The local and nonlocal thermal conductance for the voltage probe heat engine are given as follows:

$$\begin{aligned} K_{LL} &= \frac{\mathcal{L}'_{11}\mathcal{L}'_{22} - \mathcal{L}'_{21}\mathcal{L}'_{12}}{T^2\mathcal{L}'_{11}}, \quad K_{PP} = \frac{\mathcal{L}'_{11}\mathcal{L}'_{33} - \mathcal{L}'_{31}\mathcal{L}'_{13}}{T^2\mathcal{L}'_{11}}, \\ K_{LP} &= \frac{\mathcal{L}'_{11}\mathcal{L}'_{23} - \mathcal{L}'_{21}\mathcal{L}'_{13}}{T^2\mathcal{L}'_{11}}, \quad K_{PL} = \frac{\mathcal{L}'_{11}\mathcal{L}'_{32} - \mathcal{L}'_{12}\mathcal{L}'_{31}}{T^2\mathcal{L}'_{11}}. \end{aligned} \quad (\text{B8})$$

The thermal conductance for the voltage-temperature probe heat engine is

$$K_{LL} = \frac{\mathcal{L}''_{11}\mathcal{L}''_{22} - \mathcal{L}''_{21}\mathcal{L}''_{12}}{T^2\mathcal{L}''_{11}}. \quad (\text{B9})$$

The Peltier coefficient is related to the Seebeck coefficient by relation $\Pi_{ij}(\phi) = TS_{ji}(-\phi)$.

The generalized figure of merit for the voltage probe is defined as follows:

$$z_{LP}^\theta T = \frac{\theta T}{K_{LL}}, \quad z_{LP}^\theta T = \frac{\theta T}{K_{LP}}, \quad (\text{B10})$$

where $\theta = A, A', A'', B, B', C, C'$ is given as follows:

$$\begin{aligned} A &= S_{LL}(\phi)S_{LP}(\phi)G_{LL}(\phi), \\ A' &= S_{LL}(\phi)S_{LP}(-\phi)G_{LL}(\phi), \\ A'' &= S_{LL}(-\phi)S_{LP}(\phi)G_{LL}(\phi), \\ B &= S_{LP}(\phi)^2G_{LL}(\phi), B' = S_{LP}(\phi)S_{LP}(-\phi)G_{LL}(\phi), \\ C &= S_{LL}(\phi)^2G_{LL}(\phi), C' = S_{LL}(\phi)S_{LL}(-\phi)G_{LL}(\phi). \end{aligned} \quad (\text{B11})$$

Appendix C: Carnot efficiency for a three-terminal heat engine

Carnot efficiency is the upper bound of the efficiency of a thermoelectric heat engine which can be derived from the zero entropy production rate condition [30]. A voltage probe heat engine operating between temperatures $T_R < T_P < T_L$, the Carnot efficiency is defined as follows [53]:

if J_L^Q only is positive

$$\eta_{C,L} = 1 - \frac{T_R}{T_L} + \frac{J_P^Q}{J_L^Q} \left(1 - \frac{T_R}{T_P}\right), \quad (\text{C1})$$

and if both J_L^Q and J_P^Q are positive

$$\eta_{C,LP} = 1 - \frac{T_R}{T_L} \left(1 + \frac{\frac{T_L}{T_P} - 1}{1 + \frac{J_L^Q}{J_P^Q}}\right). \quad (\text{C2})$$

For a voltage-temperature probe with $J_P^Q = 0$, the Carnot efficiency is defined as

$$\eta_C = 1 - \frac{T_R}{T_L}. \quad (\text{C3})$$

One can observe that the Carnot efficiency of the voltage-temperature probe heat engine depends only on the temperatures of the left (hot) and the right (cold) reservoirs like the two-terminal heat engine. However, the Carnot efficiency is not constant for a voltage probe heat engine. It depends on the temperatures of all three reservoirs and is a function of the heat currents from the left reservoir and the probe.

-
- [1] R. Long and W. Liu, Unified trade-off optimization for general heat devices with nonisothermal processes, *Phys. Rev. E* **91**, 042127 (2015).
 - [2] P. Pietzonka and U. Seifert, Universal trade-off between power, efficiency, and constancy in steady-state heat engines, *Phys. Rev. Lett.* **120**, 190602 (2018).
 - [3] S. Krishnamurthy, S. Ghosh, D. Chatterji, R. Ganapathy, and A. K. Sood, A micrometre-sized heat engine operating between bacterial reservoirs, *Nature Physics* **12**, 1134 (2016).
 - [4] J. Roßnagel, S. T. Dawkins, K. N. Tolazzi, O. Abah, E. Lutz, F. Schmidt-Kaler, and K. Singer, A single-atom heat engine, *Science* **352**, 325 (2016).
 - [5] G. Benenti, G. Casati, K. Saito, and R. S. Whitney, Fundamental aspects of steady-state conversion of heat to work at the nanoscale, *Physics Reports* **694**, 1 (2017).
 - [6] H. van Houten, L. W. Molenkamp, C. W. J. Beenakker, and C. T. Foxon, Thermo-electric properties of quantum point contacts, *Semiconductor Science and Technology* **7**, B215 (1992).
 - [7] R. S. Whitney, Most efficient quantum thermoelectric at finite power output, *Phys. Rev. Lett.* **112**, 130601 (2014).
 - [8] R. S. Whitney, Finding the quantum thermoelectric with maximal efficiency and minimal entropy production at given power output, *Phys. Rev. B* **91**, 115425 (2015).
 - [9] R. S. Whitney, R. Sánchez, and J. Splettstoesser, Quantum thermodynamics of nanoscale thermoelectrics and electronic devices, in *Thermodynamics in the Quantum Regime: Fundamental Aspects and New Directions*, edited by F. Binder, L. A. Correa, C. Gogolin, J. Anders, and G. Adesso (Springer International Publishing, Cham, 2018) pp. 175–206.
 - [10] N. Taniguchi, Quantum control of nonlinear thermoelectricity at the nanoscale, *Phys. Rev. B* **101**, 115404 (2020).
 - [11] G. D. Mahan and J. O. Sofo, The best thermoelectric, *Proceedings of the National Academy of Sciences* **93**, 7436 (1996).
 - [12] M. S. Dresselhaus, G. Chen, M. Y. Tang, R. G. Yang, H. Lee, D. Z. Wang, Z. F. Ren, J.-P. Fleurial, and P. Gogna, New directions for low-dimensional thermoelectric materials, *Advanced Materials* **19**, 1043 (2007).
 - [13] B. Buča and T. Prosen, A note on symmetry reductions of the lindblad equation: transport in constrained open spin chains, *New Journal of Physics* **14**, 073007 (2012).
 - [14] J. Thingna, D. Manzano, and J. Cao, Dynamical signatures of molecular symmetries in nonequilibrium quantum transport, *Scientific Reports* **6**, 28027 (2016).
 - [15] D. Manzano and P. Hurtado, Harnessing symmetry to control quantum transport, *Advances in Physics* **67**, 1 (2018).
 - [16] D. Rai, O. Hod, and A. Nitzan, Magnetic field control of the current through molecular ring junctions, *The Journal of Physical Chemistry Letters* **2**, 2118 (2011).
 - [17] G. Engelhardt and J. Cao, Tuning the aharonov-bohm effect with dephasing in nonequilibrium transport, *Phys. Rev. B* **99**, 075436 (2019).
 - [18] J. Thingna, D. Manzano, and J. Cao, Magnetic field induced symmetry breaking in nonequilibrium quantum networks, *New Journal of Physics* **22**, 083026 (2020).
 - [19] Y. M. Blanter, C. Bruder, R. Fazio, and H. Schoeller, Aharonov-bohm-type oscillations of thermopower in a

- quantum-dot ring geometry, *Phys. Rev. B* **55**, 4069 (1997).
- [20] P. P. Hofer and B. Sothmann, Quantum heat engines based on electronic mach-zehnder interferometers, *Phys. Rev. B* **91**, 195406 (2015).
- [21] C. J. Lambert, H. Sadeghi, and Q. H. Al-Galiby, Quantum-interference-enhanced thermoelectricity in single molecules and molecular films, *Comptes Rendus Physique* **17**, 1084 (2016).
- [22] P. Samuelsson, S. Kheradsoud, and B. Sothmann, Optimal quantum interference thermoelectric heat engine with edge states, *Phys. Rev. Lett.* **118**, 256801 (2017).
- [23] S.-Y. Hwang, F. Giazotto, and B. Sothmann, Phase-coherent heat circulator based on multiterminal josephson junctions, *Phys. Rev. Appl.* **10**, 044062 (2018).
- [24] S. Hershfield, K. A. Muttalib, and B. J. Nartowt, Non-linear thermoelectric transport: A class of nanodevices for high efficiency and large power output, *Phys. Rev. B* **88**, 085426 (2013).
- [25] Y. Apertet, H. Ouerdane, C. Goupil, and P. Lecoeur, Irreversibilities and efficiency at maximum power of heat engines: The illustrative case of a thermoelectric generator, *Phys. Rev. E* **85**, 031116 (2012).
- [26] K. Yamamoto and N. Hatano, Thermodynamics of the mesoscopic thermoelectric heat engine beyond the linear-response regime, *Phys. Rev. E* **92**, 042165 (2015).
- [27] K. Yamamoto, O. Entin-Wohlman, A. Aharony, and N. Hatano, Efficiency bounds on thermoelectric transport in magnetic fields: The role of inelastic processes, *Phys. Rev. B* **94**, 121402 (2016).
- [28] J.-H. Jiang, Enhancing efficiency and power of quantum-dots resonant tunneling thermoelectrics in three-terminal geometry by cooperative effects, *Journal of Applied Physics* **116**, 194303 (2014).
- [29] R. S. Whitney, Thermodynamic and quantum bounds on nonlinear dc thermoelectric transport, *Phys. Rev. B* **87**, 115404 (2013).
- [30] S. Carnot, Reflections on the motive power of fire, and on machines fitted to develop that power, Paris: Bachelier **108**, 1824 (1824).
- [31] F. L. Curzon and B. Ahlborn, Efficiency of a Carnot engine at maximum power output, *American Journal of Physics* **43**, 22 (1975).
- [32] C. Van den Broeck, Thermodynamic efficiency at maximum power, *Phys. Rev. Lett.* **95**, 190602 (2005).
- [33] A. De Vos, Endoreversible thermodynamics and chemical reactions, *The Journal of Physical Chemistry* **95**, 4534 (1991).
- [34] B. Jiménez de Cisneros and A. C. Hernández, Collective working regimes for coupled heat engines, *Phys. Rev. Lett.* **98**, 130602 (2007).
- [35] B. Andresen, Current trends in finite-time thermodynamics, *Angewandte Chemie International Edition* **50**, 2690 (2011).
- [36] M. Esposito, R. Kawai, K. Lindenberg, and C. Van den Broeck, Efficiency at maximum power of low-dissipation carnot engines, *Phys. Rev. Lett.* **105**, 150603 (2010).
- [37] A. Ryabov and V. Holubec, Maximum efficiency of steady-state heat engines at arbitrary power, *Phys. Rev. E* **93**, 050101 (2016).
- [38] V. Holubec and A. Ryabov, Maximum efficiency of low-dissipation heat engines at arbitrary power, *Journal of Statistical Mechanics: Theory and Experiment* **2016**, 073204 (2016).
- [39] V. Holubec and A. Ryabov, Efficiency at and near maximum power of low-dissipation heat engines, *Phys. Rev. E* **92**, 052125 (2015).
- [40] G. Benenti, K. Saito, and G. Casati, Thermodynamic bounds on efficiency for systems with broken time-reversal symmetry, *Phys. Rev. Lett.* **106**, 230602 (2011).
- [41] M. Büttiker, Small normal-metal loop coupled to an electron reservoir, *Phys. Rev. B* **32**, 1846 (1985).
- [42] M. Büttiker, Role of quantum coherence in series resistors, *Phys. Rev. B* **33**, 3020 (1986).
- [43] M. Büttiker, Symmetry of electrical conduction, *IBM Journal of Research and Development* **32**, 317 (1988).
- [44] S. Bedkihal, M. Bandyopadhyay, and D. Segal, The probe technique far from equilibrium: Magnetic field symmetries of nonlinear transport, *The European Physical Journal B* **86**, 506 (2013).
- [45] K. Brandner and U. Seifert, Bound on thermoelectric power in a magnetic field within linear response, *Phys. Rev. E* **91**, 012121 (2015).
- [46] K. Brandner, K. Saito, and U. Seifert, Strong bounds on onsager coefficients and efficiency for three-terminal thermoelectric transport in a magnetic field, *Phys. Rev. Lett.* **110**, 070603 (2013).
- [47] K. Brandner and U. Seifert, Multi-terminal thermoelectric transport in a magnetic field: bounds on onsager coefficients and efficiency, *New Journal of Physics* **15**, 105003 (2013).
- [48] K. Saito, G. Benenti, G. Casati, and T. c. v. Prosen, Thermopower with broken time-reversal symmetry, *Phys. Rev. B* **84**, 201306 (2011).
- [49] M. Horvat, T. c. v. Prosen, G. Benenti, and G. Casati, Railway switch transport model, *Phys. Rev. E* **86**, 052102 (2012).
- [50] V. Balachandran, G. Benenti, and G. Casati, Efficiency of three-terminal thermoelectric transport under broken time-reversal symmetry, *Phys. Rev. B* **87**, 165419 (2013).
- [51] D. Sánchez and L. m. c. Serra, Thermoelectric transport of mesoscopic conductors coupled to voltage and thermal probes, *Phys. Rev. B* **84**, 201307 (2011).
- [52] R. Zhang, Q.-W. Li, F. R. Tang, X. Q. Yang, and L. Bai, Route towards the optimization at given power of thermoelectric heat engines with broken time-reversal symmetry, *Phys. Rev. E* **96**, 022133 (2017).
- [53] F. Mazza, R. Bosisio, G. Benenti, V. Giovannetti, R. Fazio, and F. Taddei, Thermoelectric efficiency of three-terminal quantum thermal machines, *New Journal of Physics* **16**, 085001 (2014).
- [54] J. Lu, Y. Liu, R. Wang, C. Wang, and J.-H. Jiang, Optimal efficiency and power, and their trade-off in three-terminal quantum thermoelectric engines with two output electric currents, *Phys. Rev. B* **100**, 115438 (2019).
- [55] Z. Sartipi and J. Vahedi, Optimal performance of voltage-probe quantum heat engines, *Phys. Rev. B* **108**, 195435 (2023).
- [56] Y. Izumida and K. Okuda, Efficiency at maximum power of minimally nonlinear irreversible heat engines, *Europhysics Letters* **97**, 10004 (2012).
- [57] Y. Izumida, K. Okuda, J. M. M. Roco, and A. C. Hernández, Heat devices in nonlinear irreversible thermodynamics, *Phys. Rev. E* **91**, 052140 (2015).
- [58] R. Long, Z. Liu, and W. Liu, Performance optimization of minimally nonlinear irreversible heat engines and refrigerators under a trade-off figure of merit, *Phys. Rev.*

- E **89**, 062119 (2014).
- [59] R. Long and W. Liu, Efficiency and its bounds of minimally nonlinear irreversible heat engines at arbitrary power, *Phys. Rev. E* **94**, 052114 (2016).
- [60] I. Iyyappan and M. Ponmurugan, General relations between the power, efficiency, and dissipation for the irreversible heat engines in the nonlinear response regime, *Phys. Rev. E* **97**, 012141 (2018).
- [61] M. Ponmurugan, Attainability of maximum work and the reversible efficiency of minimally nonlinear irreversible heat engines, *Journal of Non-Equilibrium Thermodynamics* **44**, 143 (2019).
- [62] L. Bai, L. Li, and R. Zhang, Performance optimization of irreversible heat devices in the nonlinear response regime: Insights from the ecological criterion, *Chinese Journal of Physics* **83**, 418 (2023).
- [63] R. Zhang, W. Liu, Q. Li, L. Zhang, and L. Bai, Optimal performance at arbitrary power of minimally nonlinear irreversible thermoelectric generators with broken time-reversal symmetry, *Physics Letters A* **382**, 20 (2018).
- [64] Q. Liu, W. Li, M. Zhang, J. He, and J. Wang, Efficiency bounds for minimally nonlinear irreversible heat engines with broken time-reversal symmetry, *Entropy* **21**, 717 (2019).
- [65] M. Bandyopadhyay, S. Ghosh, A. Dubey, and S. Bedkihal, Flux dependent current rectification in geometrically symmetric interconnected triple-dot aharonov-bohm interferometer, *Physica E: Low-dimensional Systems and Nanostructures* **133**, 114786 (2021).
- [66] M. Saha, B. P. Venkatesh, and B. K. Agarwalla, Quantum transport in quasiperiodic lattice systems in the presence of büttiker probes, *Phys. Rev. B* **105**, 224204 (2022).
- [67] R. Sánchez, C. Gorini, and G. Fleury, Extrinsic thermoelectric response of coherent conductors, *Phys. Rev. B* **104**, 115430 (2021).
- [68] J. Balduque and R. Sánchez, Coherent control of thermoelectric currents and noise in quantum thermocouples, *Phys. Rev. B* **109**, 045429 (2024).
- [69] Y. Aharonov and D. Bohm, Significance of electromagnetic potentials in the quantum theory, *Phys. Rev.* **115**, 485 (1959).
- [70] M. Büttiker, Y. Imry, and M. Y. Azbel, Quantum oscillations in one-dimensional normal-metal rings, *Phys. Rev. A* **30**, 1982 (1984).
- [71] A. L. Yeyati and M. Büttiker, Aharonov-bohm oscillations in a mesoscopic ring with a quantum dot, *Phys. Rev. B* **52**, R14360 (1995).
- [72] G. Haack and F. Giazotto, Efficient and tunable aharonov-bohm quantum heat engine, *Phys. Rev. B* **100**, 235442 (2019).
- [73] G. Haack and F. Giazotto, Nonlinear regime for enhanced performance of an Aharonov–Bohm heat engine, *AVS Quantum Science* **3**, 046801 (2021).
- [74] O. Entin-Wohlman and A. Aharony, Three-terminal thermoelectric transport under broken time-reversal symmetry, *Phys. Rev. B* **85**, 085401 (2012).
- [75] S. Bedkihal, M. Bandyopadhyay, and D. Segal, Flux-dependent occupations and occupation difference in geometrically symmetric and energy degenerate double-dot aharonov-bohm interferometers, *Phys. Rev. B* **87**, 045418 (2013).
- [76] J. Behera, S. Bedkihal, B. K. Agarwalla, and M. Bandyopadhyay, Quantum coherent control of nonlinear thermoelectric transport in a triple-dot aharonov-bohm heat engine, *Phys. Rev. B* **108**, 165419 (2023).
- [77] B. D’Anjou and W. A. Coish, Anomalous magnetotransport through reflection-symmetric artificial molecules, *Phys. Rev. B* **87**, 085443 (2013).
- [78] L. Onsager, Reciprocal relations in irreversible processes. ii., *Phys. Rev.* **38**, 2265 (1931).
- [79] Y. Izumida and K. Okuda, Molecular kinetic analysis of a finite-time carnot cycle, *Europhysics Letters* **83**, 60003 (2008).
- [80] Y. Izumida and K. Okuda, Numerical Experiments of a Finite-Time Thermodynamic Cycle, *Progress of Theoretical Physics Supplement* **178**, 163 (2009).
- [81] G.-Y. Yi, C. Jiang, L.-L. Zhang, S.-R. Zhong, H. Chu, and W.-J. Gong, Manipulability of the kondo effect in a t-shaped triple-quantum-dot structure, *Phys. Rev. B* **102**, 085418 (2020).
- [82] L.-L. Zhang and W.-J. Gong, Transport properties in a non-hermitian triple-quantum-dot structure, *Phys. Rev. A* **95**, 062123 (2017).
- [83] G.-Y. Yi, X.-Q. Wang, W.-J. Gong, H.-N. Wu, and X.-H. Chen, Josephson effect in a triple-quantum-dot ring with one dot coupled to superconductors: Numerical renormalization group calculations, *Physics Letters A* **380**, 1385 (2016).
- [84] Y. Meir and N. S. Wingreen, Landauer formula for the current through an interacting electron region, *Phys. Rev. Lett.* **68**, 2512 (1992).
- [85] J.-S. Wang, B. K. Agarwalla, H. Li, and J. Thingna, Nonequilibrium green’s function method for quantum thermal transport, *Frontiers of Physics* **9**, 673 (2014).
- [86] J. Fransson, *Non-Equilibrium Nano-Physics: A Many-Body Approach*, Lecture Notes in Physics (Springer Netherlands, 2010).
- [87] A. Dhar and D. Sen, Nonequilibrium green’s function formalism and the problem of bound states, *Phys. Rev. B* **73**, 085119 (2006).
- [88] S. Datta, *Electronic Transport in Mesoscopic Systems*, Cambridge Studies in Semiconductor Physi (Cambridge University Press, 1997).
- [89] U. Sivan and Y. Imry, Multichannel landauer formula for thermoelectric transport with application to thermopower near the mobility edge, *Phys. Rev. B* **33**, 551 (1986).
- [90] P. N. Butcher, Thermal and electrical transport formalism for electronic microstructures with many terminals, *Journal of Physics: Condensed Matter* **2**, 4869 (1990).
- [91] J. P. Bergfield and C. A. Stafford, Thermoelectric signatures of coherent transport in single-molecule heterojunctions, *Nano Letters* **9**, 3072 (2009).
- [92] M. Esposito, M. A. Ochoa, and M. Galperin, Quantum thermodynamics: A nonequilibrium green’s function approach, *Phys. Rev. Lett.* **114**, 080602 (2015).
- [93] M. Esposito, M. A. Ochoa, and M. Galperin, Nature of heat in strongly coupled open quantum systems, *Phys. Rev. B* **92**, 235440 (2015).
- [94] N. Seshadri and M. Galperin, Entropy and information flow in quantum systems strongly coupled to baths, *Phys. Rev. B* **103**, 085415 (2021).
- [95] N. Bergmann and M. Galperin, A green’s function perspective on the nonequilibrium thermodynamics of open quantum systems strongly coupled to baths, *The European Physical Journal Special Topics* **230**, 859 (2021).

- [96] G. E. Topp, T. Brandes, and G. Schaller, Steady-state thermodynamics of non-interacting transport beyond weak coupling, *Europhysics Letters* **110**, 67003 (2015).
- [97] T. Schmiedl and U. Seifert, Efficiency at maximum power: An analytically solvable model for stochastic heat engines, *Europhysics Letters* **81**, 20003 (2007).
- [98] M. Esposito, K. Lindenberg, and C. V. den Broeck, Thermoelectric efficiency at maximum power in a quantum dot, *Europhysics Letters* **85**, 60010 (2009).
- [99] M. Esposito, K. Lindenberg, and C. Van den Broeck, Universality of efficiency at maximum power, *Phys. Rev. Lett.* **102**, 130602 (2009).
- [100] M. C. Rogge and R. J. Haug, Two-path transport measurements on a triple quantum dot, *Phys. Rev. B* **77**, 193306 (2008).
- [101] U. Mukhopadhyay, J. P. Dehollain, C. Reichl, W. Wegscheider, and L. M. K. Vandersypen, A 2×2 quantum dot array with controllable inter-dot tunnel couplings, *Applied Physics Letters* **112**, 183505 (2018).
- [102] C.-Y. Lai, M. D. Ventra, M. Scheibner, and C.-C. Chien, Tunable current circulation in triangular quantum-dot metastructures, *Europhysics Letters* **123**, 47002 (2018).
- [103] A. Noiri, K. Kawasaki, T. Otsuka, T. Nakajima, J. Yoneda, S. Amaha, M. R. Delbecq, K. Takeda, G. Allison, A. Ludwig, A. D. Wieck, and S. Tarucha, A triangular triple quantum dot with tunable tunnel couplings, *Semiconductor Science and Technology* **32**, 084004 (2017).
- [104] M. Josefsson, A. Svilans, A. M. Burke, E. A. Hoffmann, S. Fahlvik, C. Thelander, M. Leijnse, and H. Linke, A quantum-dot heat engine operating close to the thermodynamic efficiency limits, *Nature Nanotechnology* **13**, 920 (2018).